ORIGINAL PAPER

Pyrite textures and compositions from the Zhuangzi Au deposit, southeastern North China Craton: implication for ore-forming processes

Xing-Hui Li[1,2,4] · Hong-Rui Fan[1,2,3] [ID] · Kui-Feng Yang[1,2,3] · Pete Hollings[4] · Xuan Liu[1,3] · Fang-Fang Hu[1,2,3] · Ya-Chun Cai[1]

Abstract

The Zhuangzi Au deposit in the world-class Jiaodong gold province hosts visible natural gold, and pyrite as the main ore mineral, making it an excellent subject for deciphering the complex hydrothermal processes and mechanisms of gold precipitation. Three types of zoned pyrite crystals were distinguished based on textural and geochemical results from EPMA, SIMS sulfur isotopic analyses and NanoSIMS mapping. Py0 has irregular shapes and abundant silicate inclusions and was contemporaneous with the earliest pyrite–sericite–quartz alteration. It has low concentrations of As (0–0.3 wt.%), Au and Cu. Py1 precipitated with stage I mineralization shows oscillatory zoning with the bright bands having high As (0.4–3.9 wt.%), Au and Cu contents, whereas the dark bands have low contents of As (0–0.4 wt.%), Au and Cu. The oscillatory zoning represents pressure fluctuations and repeated local fluid phase separation around the pyrite crystal. The concentration of invisible gold in Py1 is directly proportional to the arsenic concentration. Py1 is partially replaced by Py2 which occurs with arsenopyrite, chalcopyrite and native gold in stage II. The replacement was likely the result of pseudomorphic dissolution–reprecipitation triggered by a new pulse of Au-rich hydrothermal fluids. The $\delta^{34}S$ values for the three types of pyrite are broadly similar ranging from $+7.1$ to $+8.8‰$, suggesting a common sulfur source. Fluid inclusion microthermometry suggests that extensive phase separation was responsible for the gold deposition during stage II mineralization. Uranium–Pb dating of monazite constrains the age of mineralization to ca. 119 Ma coincident with a short compressional event around 120 Ma linked to an abrupt change in the drift direction of the subducting Pacific plate.

Keywords Pyrite · As–Au–Cu · Sulfur isotope · Fluid inclusion · Monazite · NanoSIMS mapping

Communicated by Othmar Müntener.

✉ Hong-Rui Fan
  fanhr@mail.iggcas.ac.cn

1 Key Laboratory of Mineral Resources, Institute of Geology and Geophysics, Chinese Academy of Sciences, Beijing 100029, China

2 College of Earth and Planetary Sciences, University of Chinese Academy of Sciences, Beijing 100049, China

3 Institutions of Earth Science, Chinese Academy of Sciences, Beijing 100029, China

4 Geology Department, Lakehead University, Ontario P7B 5E1, Canada

Introduction

The source of ore-forming fluids, the physico-chemical evolution of mineralizing systems, and the age of mineralization are critical subjects for studies of gold deposits (e.g., Peterson and Mavrogenes 2014; Chen et al. 2015; Mills et al. 2015; Ma et al. 2017). A comprehensive understanding of the components and processes of the hydrothermal fluids responsible for gold precipitation is critical for the development of enhanced exploration strategies (Barker et al. 2009; Peterson and Mavrogenes 2014; Velasquez et al. 2014; Chen et al. 2015; Tanner et al. 2016). Pyrite is the most common ore mineral in many types of gold deposit and can provide such information (e.g., Deditius et al. 2014; Tanner et al. 2016). Recent advances in spatial resolution and in situ microanalytical techniques allow us to determine the distribution of trace

elements (such as Au, As, Cu) and to probe S isotopes ($^{34}S/^{32}S$) in individual pyrite grains (Barker et al. 2009; Chen et al. 2015), thus providing an opportunity to investigate the temporal evolution of the ore-forming fluids.

The Jiaodong gold district, with a total reserve of > 4000 tons gold, is the most important gold producing region in China (Fan et al. 2016). Numerous studies using isotopes, fluid inclusions and geochronology have been completed (e.g., Yang and Zhou 2001; Fan et al. 2003; Li et al. 2012; Ma et al. 2017), but few of them investigated the geochemical and microtextural features of pyrite, the main gold-bearing mineral in the district (Yang et al. 2016). Although it has been speculated that gold can occur as both "invisible" (solid solution and nanoparticles) and visible (inclusions or fracture-filling) grains within pyrites in the district (Mills et al. 2015; Yang et al. 2016), direct evidence supporting the existence of "invisible" gold is lacking. Consequently the temporal and spatial relationships between "invisible" and native gold, that would provide critical information on the paragenesis of gold mineralization, remain largely unknown. Gold in the district is commonly associated with As in arsenian pyrite, as first recognized by Mills et al. (2015). The gold–arsenic correlation can not only help constrain the behavior of these two elements in pyrite, but can also be used to investigate gold transportation and precipitation mechanisms (Deditius et al. 2014). It is generally accepted that As modifies the surface properties of pyrite, favoring the attachment of Au sulfide complexes (e.g., Reich et al. 2005; Mikhlin et al. 2011; Deditius et al. 2014); however, the exact mechanism is enigmatic.

This study investigated the genesis of the quartz-vein mineralization in the Penglai–Qixia gold belt, which is one of three large gold belts in the Jiaodong district (Fan et al. 2007). Gold deposits in this belt, such as Heilangou, Daliuhang and Zhuangzi, are characterized by the presence of visible gold grains. The Zhuangzi gold deposit, although the smallest of the three has a relatively simple mineralization style and preserves detailed metallogenic information. We completed a geochemical and textural study based on nanometer-scale secondary ion mass spectrometry (NanoSIMS) mapping, in situ secondary ion mass spectrometry (SIMS) and multi-collector laser ablation inductively coupled plasma mass spectrometry (LA-MC-ICPMS) sulfur isotope analysis, electron probe microanalysis (EPMA), and backscatter electron (BSE) scanning microscopy analysis on zoned pyrite and pyrrhotite in the Zhuangzi deposit. In situ monazite U–Pb dating and microthermometry of fluid inclusions were also employed to constrain the age of mineralization and precipitation mechanisms. The results demonstrate a link between multi-pulse hydrothermal activities and gold precipitation, and highlight the intimate relationship between Au and As. Furthermore, "invisible" gold probably incorporated through solid solution has been identified

visually, representing a pioneering research in the Jiaodong gold district.

Geologic background

The Jiaodong district is located on the southeastern margin of the North China Craton (NCC). It comprises the Jiaobei Terrane in the northwest and the Sulu ultra-high pressure (UHP) metamorphic belt in the southeast, separated by the Wulian–Yantai Fault (Zhou et al. 2008; Fig. 1b). The Jiaobei Terrane is subdivided into the northern Jiaobei Uplift and the southern Jiaolai Basin. The Jiaobei Uplift is dominated by Precambrian metamorphic basement, including the Neoarchean Jiaodong Group, the Paleoproterozoic Jingshan and Fenzishan Groups, the Neoproterozoic Penglai Group, and Precambrian gneisses, intruded by widespread Mesozoic granitoids, whereas the Jiaolai Basin is filled with sedimentary (basal Laiyang Group at ca. 130 Ma and upper Wangshi Group at ca. 74 Ma) and volcanic rocks (central Qingshan Group at 124–98 Ma; Liu et al. 2009; Xie et al. 2012). The Sulu UHP Belt mainly consists of Neoproterozoic granitic gneisses, Triassic UHP metamorphic rocks and early Mesozoic granitoids (Zheng 2008; Xu et al. 2016).

The Jiaodong gold district underwent complex tectonic transitions due to changes in the direction and angle of subduction of the Izanagi–Pacific plate during the late Mesozoic (Sun et al. 2007). The stress field changed from transpression to extension at ~ 140 Ma, and then to transpression at ~ 125–122 Ma followed by late extension again at ~ 110 Ma (e.g., Fan et al. 2003; Sun et al. 2007; Zhu et al. 2010; Deng et al. 2015). The first stage was characterized by the NE–NNE-trending brittle-ductile shear zones with sinistral oblique reverse movements in the Late Jurassic. The second stage involved reactivation with development of brittle normal faults and magmatism in the Early Cretaceous. This was followed by sinistral strike slip due to NW–SE compression at ~ 120–110 Ma. The last extensional stage occurred at ~ 110 Ma due to NNW–SSE tension, and is characterized by normal faults and pull-apart basins (Sun et al. 2007; Deng et al. 2015).

Gold deposits in the Jiaodong district are divided into three belts from west to east, the Zhaoyuan–Laizhou, Penglai–Qixia and Muping–Rushan belts, which are controlled by second- or third-order NE–NNE-trending faults of the Tan–Lu fault system (Fig. 1b; Fan et al. 2007). These deposits, dated at 120 ± 5 Ma, are hosted by both Mesozoic granitoids and Precambrian metamorphic rocks (e.g., Yang and Zhou 2001; Fan et al. 2003; Li et al. 2012). Mineralization styles in the district, including the Linglong-type quartz-vein gold mineralization and the Jiaojia-type disseminated and stockwork gold mineralization, are thought to have formed in the same tectonic setting, but under different local
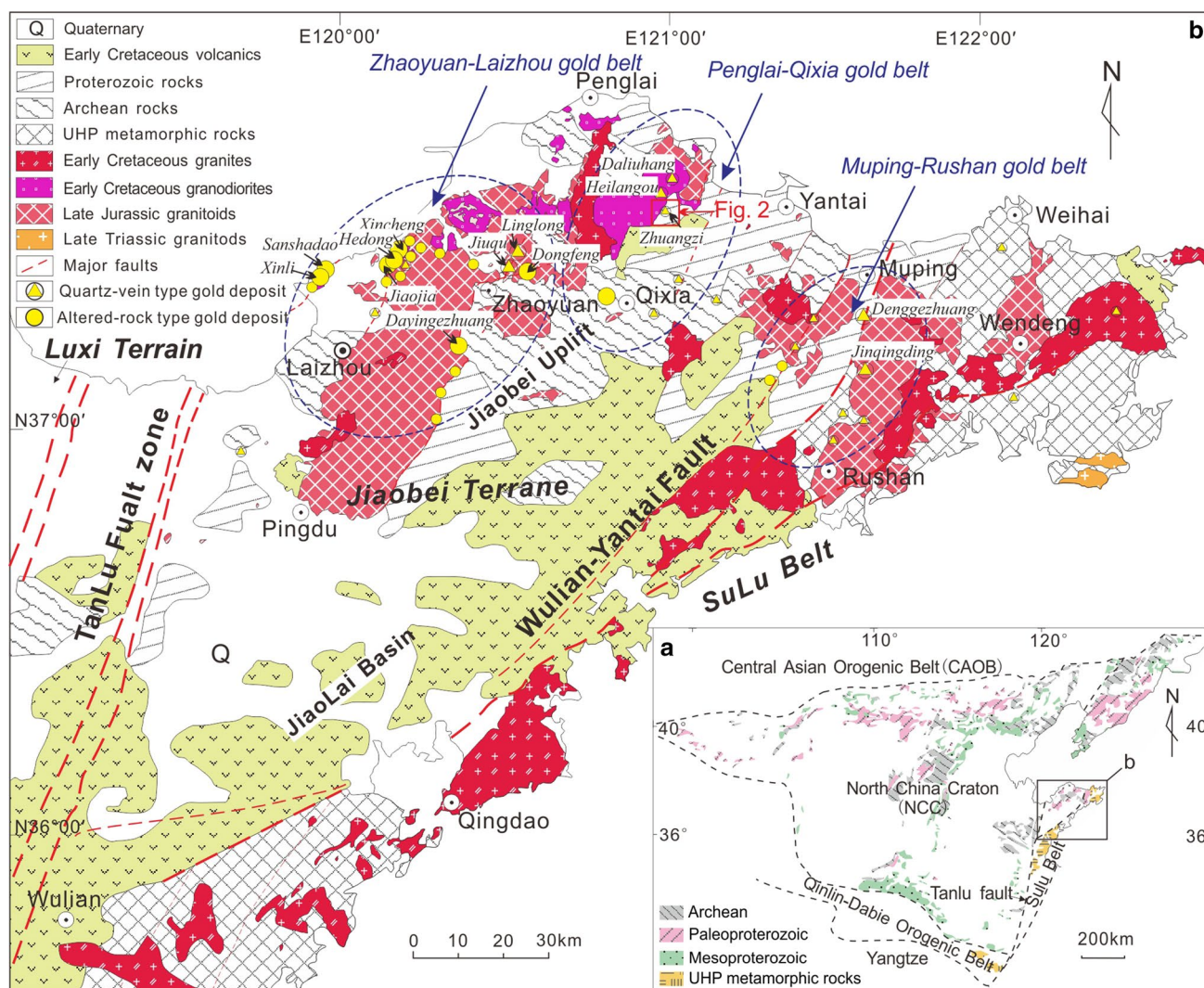
Fig. 1 **a** Simplified geological map of the North China Craton. **b** Geological map showing the distribution of the basement rocks, UHP metamorphic rocks, Mesozoic igneous rocks and gold deposits. Modified after Yang et al. (2012)

stress fields (Qiu et al. 2002; Yang et al. 2018). Compared to the Zhaoyuan–Laizhou belt which hosts over 85% of mineralization in the district, the Penglai–Qixia belt, located ~ 50 km east of the Zhaoyuan–Laizhou belt (Fig. 1b), has received much less attention, although the recent discovery of several gold deposits has resulted in new exploration. The belt mainly contains auriferous quartz-vein type deposits, associated with few disseminated-stockwork types (Qiu et al. 2002).

Deposit geology

The Zhuangzi gold deposit is located in the northern section of the Penglai–Qixia belt. Several auriferous quartz veins have been identified in the deposit, controlled by

NNE-trending fractures (e.g., F1, F8, F9; Fig. 2) and cut by the NW-trending Xishipeng–Wazi fault. The most economic Vein I is mainly hosted in the Paleoproterozoic Lugezhuang formation of the Jingshan Group, which is dominated by biotite schist and biotite granulite. The other veins are hosted in the Paleoproterozoic gneisses and Early Cretaceous Guojialing granodiorites (Fig. 2). Ore bodies in the Vein I system strike NNE 15°–20°, sub-parallel to lithological layers (Fig. 3a), and dip NW 44°–52°, with a length of 600 m and varying thicknesses of 0.2–2.1 m. Gold grades in the ore bodies are 5.0–7.6 g/t, reaching 104.0 g/t where visible gold is present in hand specimens (e.g., Fig. 3f).

Vein I comprises a proximal alteration zone of sericite, quartz, pyrite and relict biotite and an inner auriferous laminated quartz vein. The alteration is associated with a strong foliation (Fig. 4a), suggesting that the rock underwent
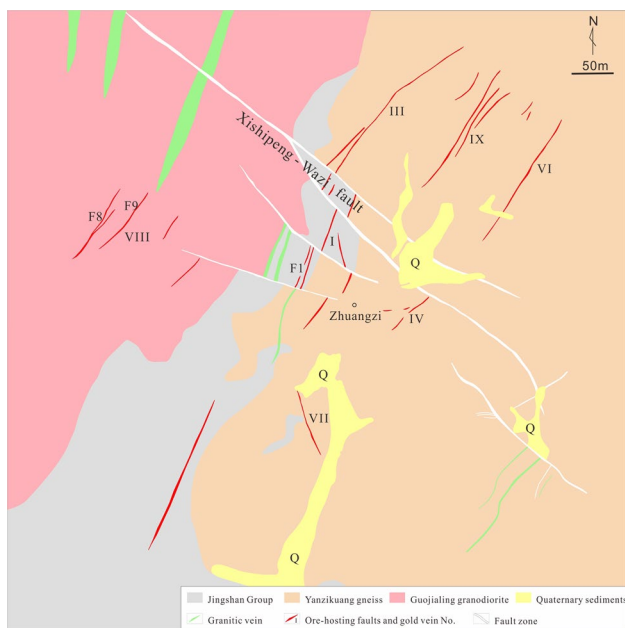
Fig. 2 Geologic map of the Zhuangzi gold deposit, showing the distribution of the ore veins

pyrite–sericite–quartz alteration followed by or simultaneously with mylonitization. The inner auriferous laminated quartz veins generally enclose lenticular clasts of altered rocks, and contain laminations of altered minerals or pyrite (Figs. 3b, d, e, 4b), suggesting synchronous, progressive sinistral shear during mineralization (Davis and Hippertt 1998). Evidence for sinistral shear is also proved by the development of slickensides on the lamination planes. The major ore minerals comprise gold, pyrite and pyrrhotite with minor accessory arsenopyrite, chalcopyrite and galena, whereas the main gangue minerals are quartz, sericite, dolomite and calcite.

A three-stage sequence of vein mineralization can be recognized at Zhuangzi (Fig. 3a, c–e). Low-grade stage I is characterized by the assemblage of gold + quartz + pyrite (Fig. 4e). In this stage, large amounts of euhedral or elongated pyrites occur as pyrite veins or quartz-pyrite veins with rare fine-grained quartz and submicron gold particles. These veins were generally altered and overprinted by the later hydrothermal fluids. Stage II is characterized by the assemblage of dolomite + arsenopyrite + pyrrhotite + pyrite + quartz + gold (Fig. 4b, c, f–i). It is defined by laminated quartz veins with variable grain sizes. The fine-grained polygonal quartz grains are adjacent to the laminae or along grain margins, whereas coarse elongate grains occur in the centre of the veins with their maximum dimensions at high angles to vein margins (Fig. 4c). Some of the fine-grained quartz has undergone dynamic recrystallization and occurs as shear lenses (Fig. 4b), suggesting contemporaneous deformation. Pyrite grains in this stage display

different textures, including round compact pyrite, concentrically zoned pyrite, and small pyrite grains with euhedral and subhedral morphologies. Small amounts of arsenopyrite grains associated with pyrite also precipitated in this stage (Fig. 4g). Pyrrhotite grains coexist with pyrite or fill in the fractures and vugs (Fig. 4h, i). Minor chalcopyrite and monazite occur along fractures and grain boundaries of pyrite or as irregular inclusions. Native gold either associated with pyrite or between quartz grains results in the high Au grades of this stage (as much as 104 g/t). Stage III is characterized by calcite veins which are bedding-parallel or cut earlier veins, marking the last stage of mineralization (Figs. 3e, 4a).

Sampling and analytical techniques

Petrographic studies were carried out on representative samples which were mainly collected from the Vein I. Pyrite and pyrrhotite grains for textural and geochemical analyses were investigated using field emission scanning electron microscope (FESEM), EPMA, NanoSIMS mapping, and SIMS and LA-MC-ICPMS sulfur isotope analysis. Necessary fluid inclusion studies in quartz and LA-ICPMS U–Pb dating on hydrothermal monazite were also conducted. All the experiments except for LA-MC-ICPMS sulfur isotope analysis on pyrrhotite were conducted at the Institute of Geology and Geophysics, Chinese Academy of Sciences (IGGCAS) in Beijing.

Textural and geochemical analyses

Textural characterization of the mineral phases was performed using a Nova NanoSEM 450 FESEM equipped with an X-MAXN80 Energy Dispersive X-ray Spectrometer (EDS). Images were acquired in BSE mode with an accelerating voltage of 15 kV and a primary beam current of 20 nA.

Major element compositions of representative pyrite, pyrrhotite and gold crystals were collected on a JEOL JXA-8100 electron microprobe, with a focused beam diameter of 5 μm, an accelerating voltage of 20 kV and a beam current of 10 nA. Calibration standards used were pyrite for S and Fe, chalcopyrite for Cu, galena for Pb, and alloy or pure metal for As, Co, Ni, Ag and Au. The detection limits for each element were As (231 ppm), Fe (111 ppm), S (99 ppm), Pb (598 ppm), Cu (210 ppm), Zn (226 ppm), Co (112 ppm), Ni (120 ppm), Ag (253 ppm) and Au (614 ppm). Iron, S, As and Au in oscillatory-zoned pyrite were also mapped using a Cameca SXFiveFE electron microprobe, with an accelerating voltage of 20 kV and a beam current of 40 nA.

Trace elemental mapping of pyrite was performed using a Cameca NanoSIMS 50L. Samples were polished and coated with carbon for conductivity at high voltage. A Cs$^+$ beam current of ~7–10 pA with a diameter of 250 nm was
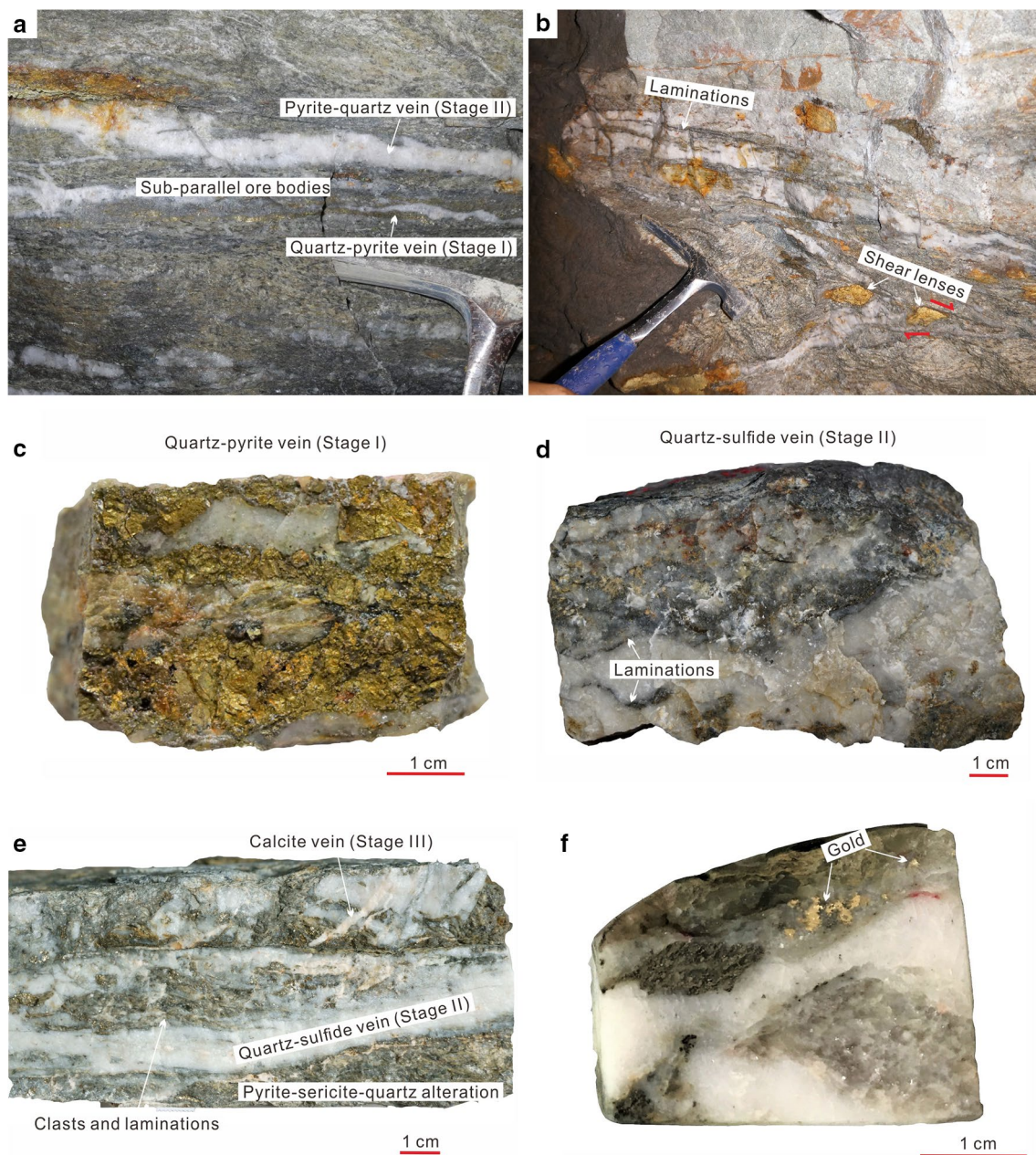
Fig. 3 Photographs of ore veins and hand specimens showing vein mineralization. **a** Bedding-parallel ore bodies. **b** Laminations and shear lenses at the bottom of the ore bodies, indicating a visually opposite shearing direction. **c** Stage I quartz-pyrite vein. **d** Stage II quartz-sulfide vein, containing laminations. **e** Stage III calcite vein, cutting quartz-sulfide veins and altered rocks. **f** Visible gold grains at Stage II

rastered across the sample surface. Before image acquisition, the selected area $(50 \times 50\ \mu m^2)$ was sputtered with a high intensity beam of 1 nA for ~2 min to remove the coating and to implant enough Cs^+ into the sample surface to stabilize the yield of the secondary ions. Images, with a pixel resolution of 256×256, were recorded simultaneously from the secondary ions ^{34}S, ^{80}Se, $^{63}Cu^{32}S$, $^{75}As^{32}S$, ^{197}Au, $^{208}Pb^{32}S$. Peaks were calibrated using arsenopyrite for AsS, chalcopyrite for CuS, galena for PbS, $FeSe_2$ for Se, and metallic Au.

In situ SIMS sulfur isotope (^{32}S, ^{33}S and ^{34}S) analysis of pyrites from different mineralization stages was performed using a Cameca IMS-1280. The Cs^+ primary ion beam was accelerated at 10 kV, with an intensity of 2.5 nA. The beam was scanned over ~25 $\mu m \times 25\ \mu m$ to reduce the depth of crater during analysis. Each analysis incorporates a pre-sputtering of 30 s, 60 s of automated centering of secondary ions, followed by 160 s integrating sulfur isotope signals. Sonora pyrite was used as a running standard for sulfur
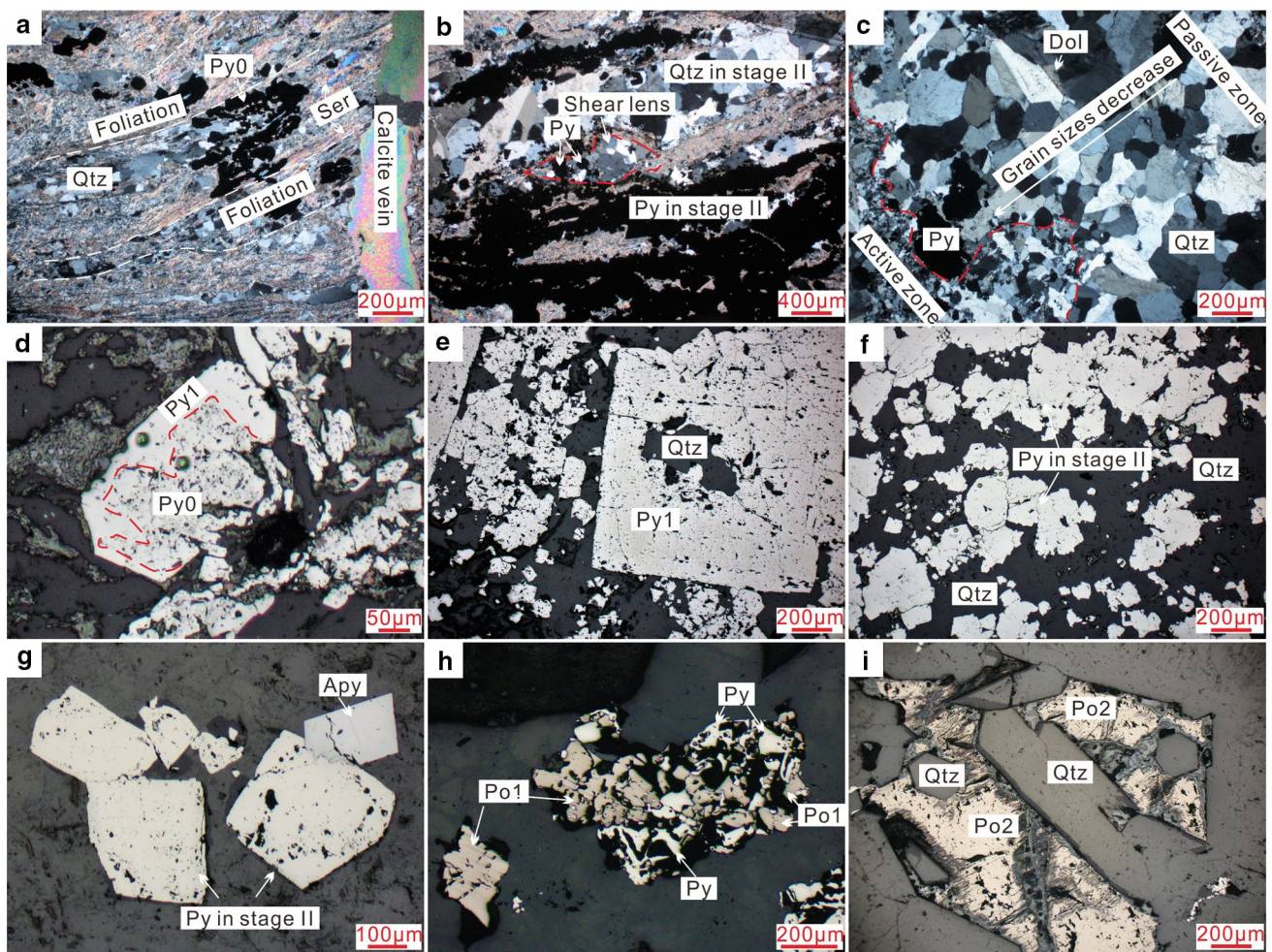
Fig. 4 Thin section microphotographs of Zhuangzi ore. **a** Mineral assemblages and foliation in the altered rock cut by a calcite vein. **b, c** Shear lens and recrystallized quartz crystals in the active zone at stage II, showing evidence of shear deformation. **d** Pyrite crystals in the pyrite–sericite–quartz alteration stage. **e** Pyrite crystals in stage (I) **f–i** Pyrite, arsenopyrite, breakdown-resulted and vug-filling pyrrhotite in stage (II). *Qtz* Quartz, *Py* pyrite, *Ser* sericite, *Apy* arsenopyrite, *Po* pyrrhotite

isotope analysis and was analyzed two or three times every six-to-eight analyses. The quality of the analyses was monitored by comparing to reference values of Sonora standard ($\delta^{34}S_{VCDT}$: $+1.61$ ‰; and $\delta^{33}S_{VCDT}$: $+0.83$ ‰; Farquhar et al. 2013). Detailed operating conditions, procedures, and data reduction are described by Chen et al. (2015).

We also chose ten pyrrhotite spots for sulfur isotope measurements using a Nu Plasma II MC-ICPMS, equipped with a Resonetics-S155 excimer ArF laser ablation system at the State Key Laboratory of Geological Processes and Mineral Resources, China University of Geosciences, Wuhan. The diameter of laser beam was 33 μm with a repetition rate of 10 Hz, and the ablation process was set to last for 40 s. Standard-sample bracketing was used to determine the $\delta^{34}S$ values of samples throughout the analytical sessions. The true sulfur isotope ratio was calculated by correction for instrumental mass bias by linear interpolation between the biases calculated from two neighboring standard analyses. The analytical precision (1σ) was about ± 0.1 per mil. Detailed analytical conditions and procedures can be seen in Zhu et al. (2017).

Monazite U–Pb dating

Monazite from ores (mainly in stage II) was selected for in situ LA-ICPMS U–Pb dating with an Agilent Q-ICPMS equipped with a Geolas 193 nm excimer laser ablation system. Analyses were conducted with a spot size of 35 μm and a repetition rate of 8 Hz. Each analysis incorporated a background acquisition of approximately 20 s followed by 45 s data acquisition. Monazite 44069 and Madagascar 1 were used as external and monitor standards to correct the U/Pb and Th/Pb fractionation and the instrumental mass discrimination. The corresponding reference ages for these

two standards are 424.9 ± 0.5 Ma for 44069 (Aleinikoff et al. 2006) and 524.8 ± 3.7 Ma for Madagascar 1 (Liu et al. 2012). Detailed operating conditions and the data reduction processes are described by Liu et al. (2012). The software package GLITTER 4.0 was used to reduce the raw U–Pb data. Considering the high common Pb compositions of the analyzed monazite, a Tera–Wasserburg Concordia diagram was plotted to obtain the $^{206}Pb/^{238}U$ age (Tera and Wasserburg 1972). The upper intercept represents the initial $^{207}Pb/^{206}Pb$ ratios, and the lower intercept presents the age for monazite formation. Using the 207-correction method, the calibrated $^{206}Pb/^{238}U$ ages were then used to calculate a weighted average age. All the weighted mean $^{206}Pb/^{238}U$ ages and $^{207}Pb/^{206}Pb$–$^{206}Pb/^{238}U$ diagrams were calculated and plotted with Isoplot (v3.75; Ludwig 2012).

Microthermometry and Raman spectroscopy

Microthermometric measurements on fluid inclusions were carried out using a Linkam THMS 600 programmable heating/freezing stage combined with a Zeiss microscope at IGGCAS. The stage was calibrated using synthetic fluid inclusions supplied by FLUID INC. through calibration against the triple-point of pure CO_2 (-56.6 °C), the freezing point of water (0.0 °C) and the critical point of water (374.1 °C). Most measurements were carried out at a heating rate of 0.2–0.4 °C/min. Carbonic phase melting (Tm_{CO_2}) and clathrate melting (Tm_{clath}) were determined by temperature cycling (Roedder 1984; Diamond 2001). A heating rate of 0.1–0.2 °C/min was adopted near phase transformations. The precision of measurements was ± 0.2 °C at temperatures below 30 °C and ± 2 °C at temperatures above 30 °C. The compositions of fluid inclusions, including vapor, fluid and daughter minerals, were identified using a LabRam HR800 Raman microspectrometer. The exciting radiation was provided by an argon ion laser with a wavelength of 532 nm and a source power of 44 mW. The spectral range falls between 100 cm^{-1} and 4000 cm^{-1} for the analyzed CO_2, N_2, and CH_4.

Results

Textures and geochemistry of pyrite and pyrrhotite

Based on optical characteristics, BSE observation and EPMA, three types of pyrite were recognized. The complete dataset of major element and sulfur isotopic compositions is given in Supplementary Table 1.

Pyrite 0 (Py0) occurs as anhedral, elongated crystals often parallel to bedding. Numerous randomly oriented silicate inclusions dominated by sericite and quartz were observed within Py0. The Py0 clusters commonly occur in alteration zones, whereas corroded Py0 grains often occur as inclusion-rich cores overgrown by Py1 and Py2 (Figs. 4a, d, 5a, b). This suggests that Py0 is the earliest pyrite accompanying the pyrite–sericite–quartz alteration. The average major element composition of Py0 is S = 52.9 ± 0.6 wt.% and Fe = 46.1 ± 0.4 wt.% (Supplementary Table 1; Fig. 6a). Concentrations of As are relatively low (0–0.3 wt.%), and most of Au contents are below the EPMA detection limit although values up to 0.24 wt.% were observed. The concentrations of Ag are near or below the detection limit of the EPMA.

Pyrite 1 (Py1), with rare or no silicate inclusions, commonly overgrows Py0 and sometimes has rims of Py2. It occurs as coarse euhedral–subhedral grains with oscillatory zoning (Figs. 5c, 7a), or inherits the anhedral appearance of Py0 with irregular oscillatory zoning (Fig. 5b). The oscillatory zoning is characterized by a rhythmic alternation of bright bands with high As (0.4–3.9 wt.%), low S (49.6–52.0 wt.%) and dark bands with low As (0-0.4 wt.%), high S (51.9–53.0 wt.%) in BSE images (Figs. 6a, c, 7a–c). Band with fine arsenopyrite inclusions surrounding the irregular oscillatory zoning indicates a higher As content in the hydrothermal fluid. Some Py1 grains without Py2 rims are accompanied with fine quartz crystals and surrounded by later coarse quartz veins indicating Py1 precipitated during stage I mineralization. The average major element composition of Py1 is S = 51.7 ± 1.1 wt.% and Fe = 45.6 ± 0.5 wt.% (Supplementary Table 1; Fig. 6a). Sulfur and arsenic from the oscillatory-zoned Py1 show a strong linear negative correlation (Fig. 6a; $R^2 = -0.77$), suggesting that arsenic substitutes for sulfur as $Fe(As_xS_{1-x})_2$ in the structure of pyrite (Fleet et al. 1989). The concentrations of Au are mostly below the detection limit of EPMA but with values reaching up to 0.29 wt.% (Supplementary Table 1).

Pyrite 2 (Py2) occurs either as subhedral to euhedral rims or as anhedral to subhedral clusters without zoning (Fig. 5b–d). It shows paragenetic relationships with rhombic arsenopyrite grains (Fig. 4g), is associated with stage II quartz grains, commonly overgrows Py1 and cements earlier pyrite grains together. Sharp boundaries and corrosion textures are present between Py1 and Py2. Pyrite grains within the shear lens in Fig. 4b have Py2 rims (Fig. 5d). These characteristics suggest that Py2 formed during stage II mineralization accompanied by shearing deformation. The average major element composition of Py2 is S = 52.7 ± 0.6 wt.% and Fe = 46.0 ± 0.3 wt.% (Supplementary Table 1; Fig. 6a). Py2 has lower concentrations of As, causing the dark appearance in BSE images. Concentrations of Au are near or below the detection limit of the EPMA.

Rarely Py0, Py1 and Py2 grains break down into small, irregular-shaped pyrrhotite (Po1; Fig. 4h). Together with the quartz vug-filling pyrrhotite (Po2; Fig. 4i), it suggests a change in fluid composition in stage II mineralization. EPMA results show compositional differences between the breakdown-resulted Po1 and the vug-filling Po2
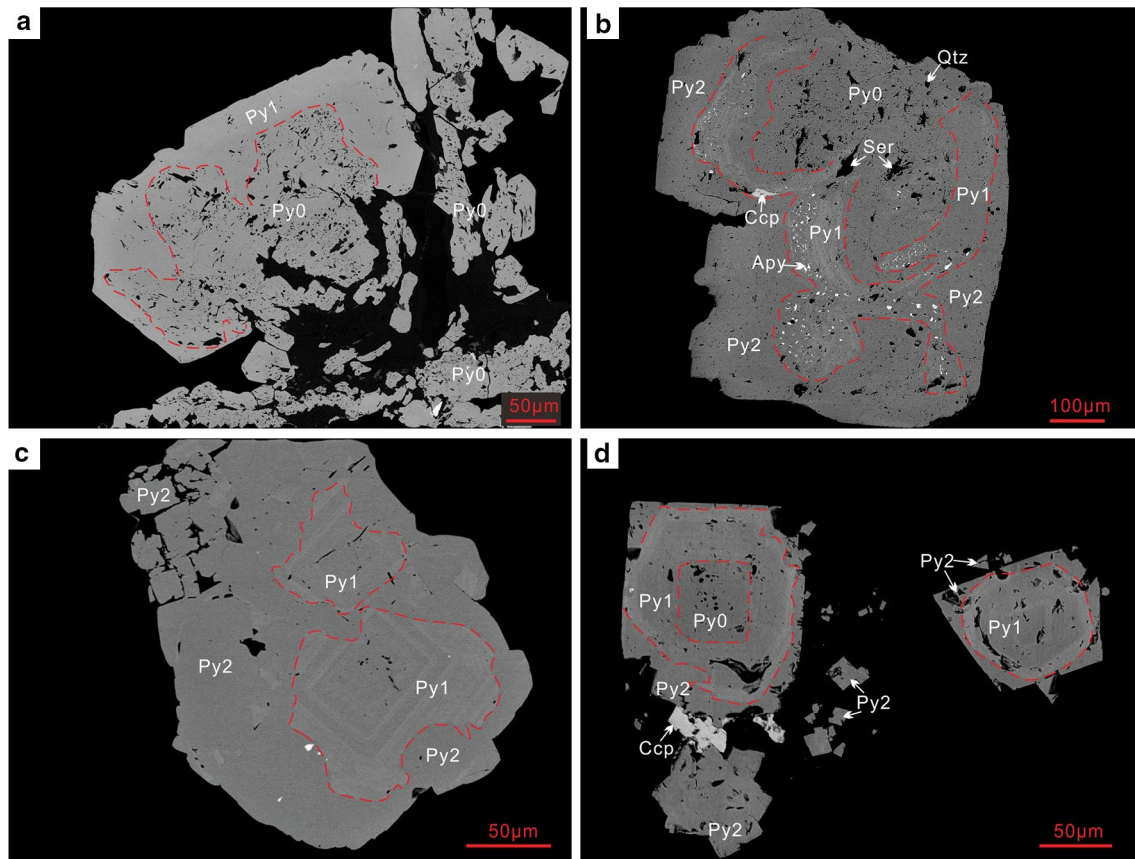
Fig. 5 BSE images of the three pyrite types. **a** Py0 with irregular shape and numerous silicate inclusions. **b** Pyrite grain comprised of Py0, Py1 and Py2. Py1 has irregular oscillatory zoning and an outermost band with fine arsenopyrite inclusions. **c** Py1 with characteristic zoning overgrown by Py2. Py2 also occurs as independent crystals. **d** Pyrite grains present in the shear lens in Fig. 4b have Py2 rims, indicating the effect of shearing deformation on Py2. *Py* Pyrite, *Ccp* chalcopyrite

(Supplementary Table 1; Fig. 6b). On the diagram of S (wt.%) versus Fe (wt.%), Po1 points distribute irregularly consistent with them having formed by the breakdown of other minerals, whereas Po2 shows a liner trend consistent with direct precipitation from hydrothermal fluids (Fig. 6b). The pyrrhotite has remarkably high concentrations of Au with most of data falling between 0.08 wt.% and 0.34 wt.%.

The $\delta^{34}S$ values of all three pyrite generations are broadly similar with a restricted range from $+7.1$ to $+9.4\ ‰$, with most data concentrating between $+7.1$ and $+8.8\ ‰$ (Supplementary Table 1; Fig. 6c). Note that slight intracrystalline $\delta^{34}S$ variation exists from core to rim (Fig. 6d). Two-sigma standard error values are between 0.08 ‰ and 0.18 ‰. The $\delta^{34}S$ values of pyrrhotite are slightly lower than that of pyrite with a small variation from $+6.5$ to $+7.7\ ‰$ (Supplementary Table 1; Fig. 6c). The sulfur isotopic composition of pyrite and pyrrhotite is consistent with pyrite and pyrrhotite that precipitated from the same hydrothermal fluid (e.g., Li et al. 2017).

Trace element distribution in pyrite

NanoSIMS mapping with submicron resolution shows that the pyrite has systematic zoning of As, Au and Cu (Fig. 7d–f), weak variation of ^{34}S, but homogeneous or no Pb and Se. The core of the grain consists of Py0 with low concentrations of trace elements. Py1 is the main body of this grain and has oscillatory-zoned As, Au and Cu which closely mimic each other (Fig. 7d–h). Zoning is sharply defined and is clearly visible as alternating broad bands of varying colors. The bright zones are enriched in As, Au and Cu in comparison to the darker zones, and these elements reach their highest concentrations in the outermost zone of Py1 (Py1f) which was corroded by later hydrothermal fluids. Fine zoning is visible inside the bright broad zones and also shows oscillatory-zoned As, Au and Cu. Py2 forms a thin, cubic rim, with low concentrations of As, Au and Cu. A slight increase in Cu concentration toward the margin of the grain is likely due to "edge effect" during the NanoSIMS analysis (Fig. 7g).
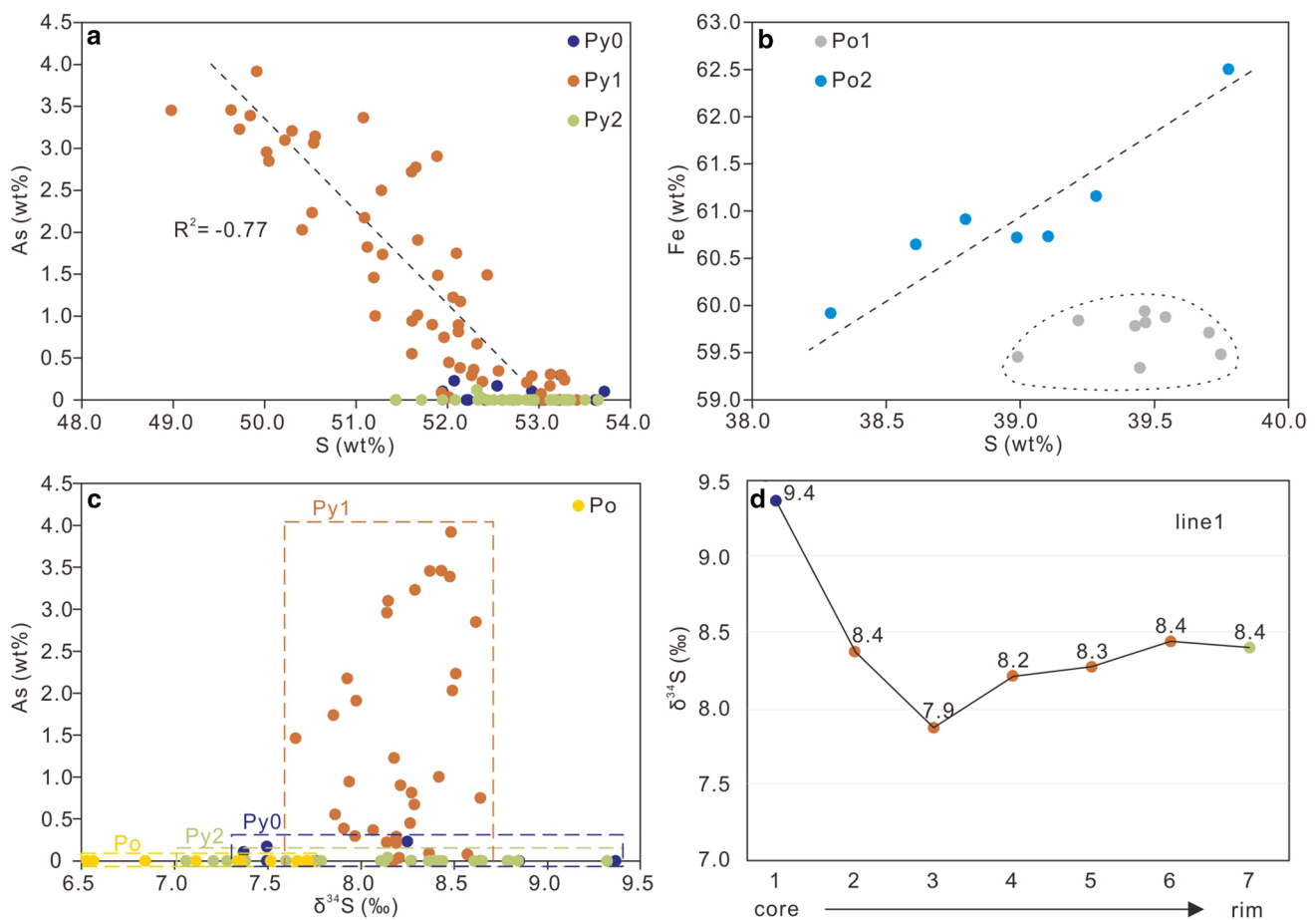
Fig. 6 Elemental abundance and $\delta^{34}S$ value diagrams for pyrite and pyrrhotite. **a** As vs. S plot for pyrite. **b** Fe vs. S plot for pyrrhotite. **c** As vs. $\delta^{34}S$ plot. **d** $\delta^{34}S$ values from core to rim in a zoned pyrite crystal

Gold occurrence and fineness

Textural and geochemical results show that both invisible and native gold occur as follows: (1) invisible gold occurs in the bright bands of Py1 (Fig. 7e); (2) native gold is mostly in close association with Py2, pyrrhotite and dolomite grains, generally along grain margins, hosted in the associated minerals, or filling fractures that crosscut pyrite crystals (Fig. 8a–f); and (3) free gold grains are in quartz veins (Figs. 3f, 8a, c). In addition, fine silver and arsenopyrite grains are present as inclusions in the outermost bands of Py1 (Fig. 8f). The native gold and free gold grains with variable sizes up to centimeter long, represent the most economic mineralization. Some native gold grains have submicron-sized inclusions of As-poor pyrite. Paragenetic relationships suggest that the precipitation of native gold grains was near-simultaneous with Py2 crystallization during stage II mineralization. EPMA data indicate that the gold grains occur mostly as electrum (Ag > 20 wt.%; Hough et al. 2009) with average Au of 77.4 ± 3.8 wt.% and Ag of 22.6 ± 3.8 wt.%. The calculated gold fineness [1000Au/(Au + Ag)] for electrum grains is 708–834, which is lower than that typical for orogenic deposits worldwide (> 900; Velasquez et al. 2014).

Monazite U–Pb geochronology

The in situ U–Pb dating analyses of 22 spots on monazite grains are presented in Table 1. Most of the analyzed monazite grains were intergrown with or enclosed in Py2 grains, thus their crystallization ages can represent the timing of gold deposition. The U–Pb data cluster on the Tera–Wasserburg Concordia diagram, and give a lower intercept age of 119.4 ± 3.9 Ma (MSWD = 0.8). The initial $^{207}Pb/^{206}Pb$ data are 0.879 ± 0.020. The ^{207}Pb-corrected weighted mean $^{206}Pb/^{238}U$ age is 119.0 ± 3.1 Ma (n = 22, MSWD = 0.7) which is consistent with the lower intercept age (Fig. 9).
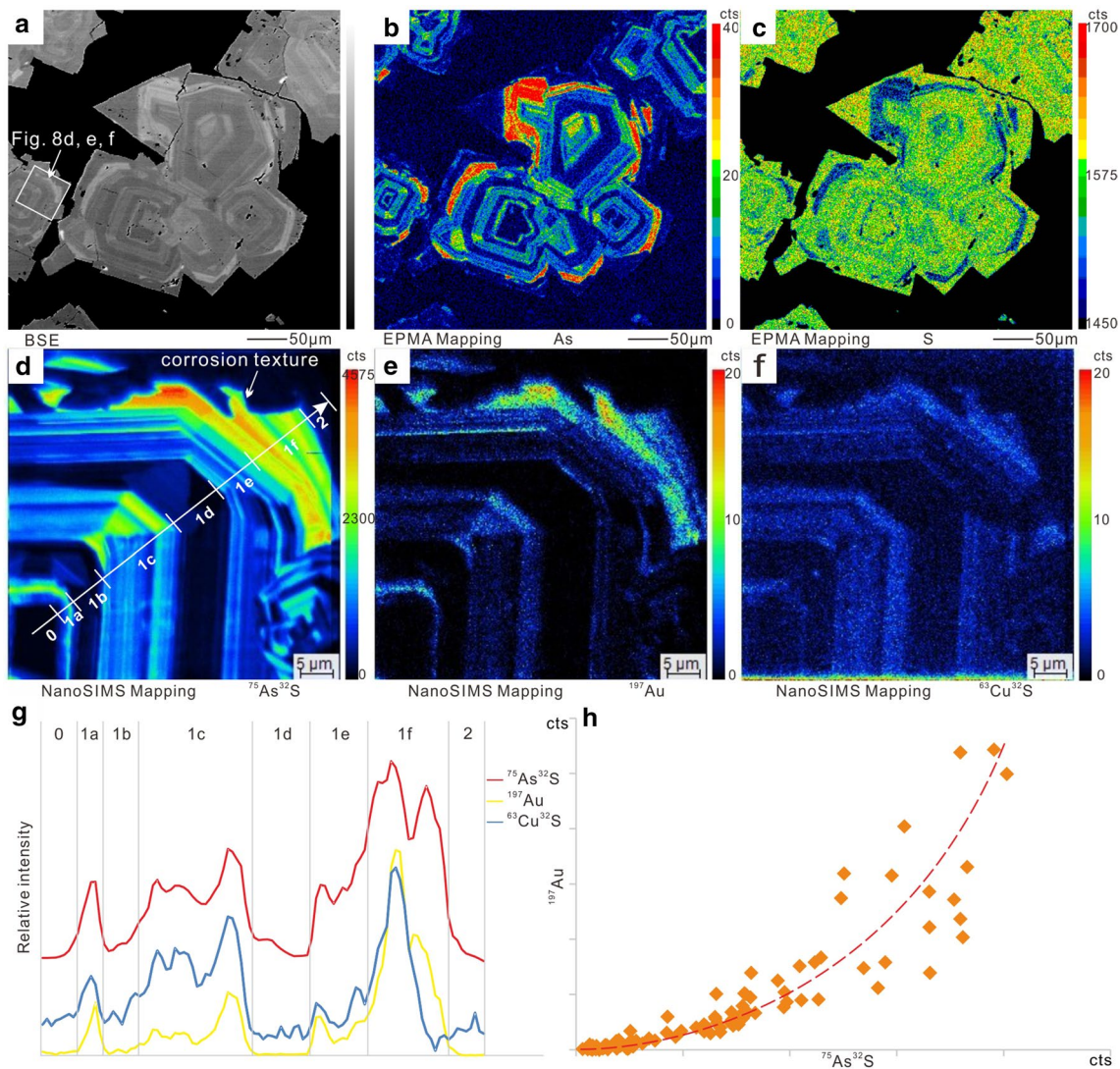
Fig. 7 EPMA and NanoSIMS maps of elemental variation in pyrite. **a** BSE images of the selected pyrite. **b, c** As and S variations, revealed by EPMA maps, respectively. **d–f** $^{75}As^{32}S$, ^{197}Au, and $^{63}Cu^{32}S$ variations from Py0 core to Py2 rim, revealed by NanoSIMS maps, respectively. **g** Variation of counting signals for $^{75}As^{32}S$, ^{197}Au, and $^{63}Cu^{32}S$ by NanoSIMS mapping. **h** Plot of counting signals for ^{197}Au vs. $^{75}As^{32}S$ by NanoSIMS mapping

Fluid inclusions

Petrography and types of fluid inclusions

Four types of fluid inclusions were distinguished in quartz based on their petrographic characteristics at room temperature and laser Raman spectroscopy: vapor-rich (> 90 vol.% CO_2 vapor, type I), $H_2O–CO_2–NaCl$ (type II), $H_2O–NaCl$ (type III), and daughter mineral-bearing $H_2O–CO_2–NaCl$ (type IV) fluid inclusions.

Type I consists of mono-phase CO_2 inclusions and two-phase $H_2O–CO_2–NaCl$ inclusions containing > 90 vol.% vapor (Fig. 10a). They are usually dark with ellipsoidal, rounded or negative crystal morphologies, ranging from 3

to 13 µm in diameter. Most of these inclusions coexist with type IIa, IIb, IIc and IIIa inclusions in quartz grains from both stage I and stage II (Fig. 10i–l).

Type II inclusions can be further divided into three subtypes, containing two-phase with 60–40 vol.% carbonic phase ($VCO_2 + LH_2O$, type IIa), two-phase with 40–20 vol.% carbonic phase (type IIb) and three-phase ($VCO_2 + LCO_2 + LH_2O$, type IIc) inclusions at room temperature with varying sizes from 5 to 22 µm. Type II inclusions commonly occur as assemblages, in cluster or in isolation in quartz in both stage I and stage II (Fig. 10b–d, h).

Type III inclusions are one-phase (LH_2O, type IIIa) or two-phase ($LH_2O + VCO_2$, type IIIb) liquid-rich aqueous inclusions (Fig. 10e, f). They display irregular, ellipsoidal
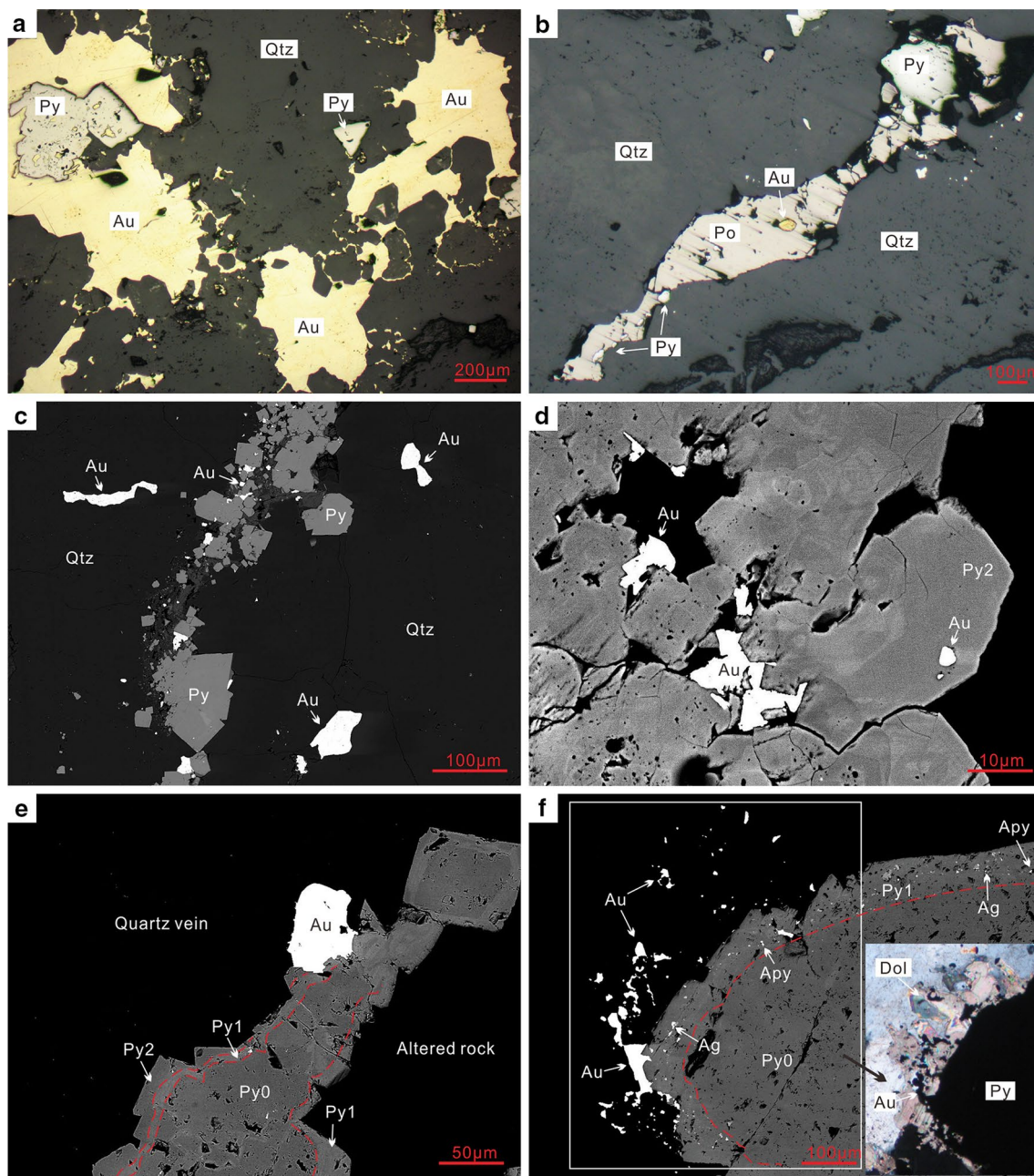
Fig. 8 Reflected light and BSE images showing visible gold grains. **a** Free gold in quartz veins. **b** Native gold inclusion in pyrrhotite. **c–e** Native gold in fractures of Py2, at grain margin of quartz or Py2, and as inclusions in Py2. **f** Native gold accompanied by dolomite. *Qtz* Quartz, *Py* pyrite, *Au* gold, *Ag* silver, *Apy* arsenopyrite, *Po* pyrrhotite, *Dol* dolomite

or negative crystal morphologies and range from 3 to 25 µm in length. Type IIIa commonly coexists with type I, type IIa and/or type IIb fluid inclusions, whereas primary type IIIb fluid inclusions mainly occur in clustered quartz from late stage II and distribute as assemblages.

Type IV inclusions are characterized by the presence of a calcite crystal within the H_2O–CO_2–NaCl fluid inclusion (Fig. 10g). They are irregular or negative crystal in shape

with 3–15 µm in diameter and occur as clusters or isolated individuals in samples from stage II.

Fluid inclusion microthermometry and Raman spectroscopic results

Microthermometric data were obtained from 183 fluid inclusions and in most case the measurements were conducted

Table 1 Results of in situ LA-ICPMS U–Pb dating on hydrothermal monazite in the Zhuang gold deposit

Spot no.	Isotopic ratios								[207]Pb-corr.Age/Ma	
	[207]Pb/[206]Pb	1σ	[207]Pb/[235]U	1σ	[206]Pb/[238]U	1σ	[208]Pb/[232]Th	1σ	[206]Pb/[238]U	1σ
1	0.0587	0.0304	0.1530	0.0783	0.0189	0.0015	0.0058	0.00011	119	10
2	0.0508	0.0120	0.1275	0.0296	0.0182	0.0009	0.0056	0.00007	116	6
3	0.1528	0.0179	0.4386	0.0467	0.0208	0.0010	0.0060	0.00009	116	7
4	0.0818	0.0153	0.2346	0.0430	0.0208	0.0009	0.0061	0.00009	128	5
5	0.2044	0.0351	0.6758	0.1046	0.0240	0.0018	0.0057	0.00006	124	11
6	0.4894	0.0377	2.9860	0.1563	0.0443	0.0026	0.0063	0.00010	132	16
7	0.2594	0.0315	0.8067	0.0825	0.0226	0.0015	0.0057	0.00006	108	10
8	0.5297	0.0269	2.8410	0.0913	0.0389	0.0017	0.0069	0.00010	105	10
9	0.3198	0.0313	1.0727	0.0827	0.0243	0.0015	0.0058	0.00009	105	9
10	0.1351	0.0468	0.3850	0.1267	0.0207	0.0023	0.0056	0.00008	118	14
11	0.2760	0.0311	0.9604	0.0910	0.0252	0.0016	0.0066	0.00011	117	10
12	0.0942	0.0150	0.2469	0.0375	0.0190	0.0010	0.0067	0.00040	115	6
13	0.0614	0.0131	0.1615	0.0338	0.0191	0.0008	0.0074	0.00148	120	5
14	0.1348	0.0112	0.3858	0.0301	0.0208	0.0006	0.0067	0.00014	119	4
15	0.5715	0.0183	3.9674	0.0802	0.0504	0.0014	0.0197	0.00035	119	9
16	0.4270	0.0361	2.2720	0.1394	0.0386	0.0023	0.0061	0.00007	134	15
17	0.3010	0.0181	1.1614	0.0558	0.0280	0.0011	0.0063	0.00011	124	7
18	0.3270	0.0287	1.2561	0.0871	0.0279	0.0016	0.0058	0.00008	118	10
19	0.5113	0.0344	3.2936	0.1469	0.0467	0.0025	0.0066	0.00009	132	13
20	0.4217	0.0200	1.8789	0.0610	0.0323	0.0012	0.0062	0.00007	114	7
21	0.2482	0.0206	0.8959	0.0635	0.0262	0.0012	0.0084	0.00022	127	7
22	0.1358	0.0303	0.3968	0.0840	0.0212	0.0015	0.0063	0.00008	121	9
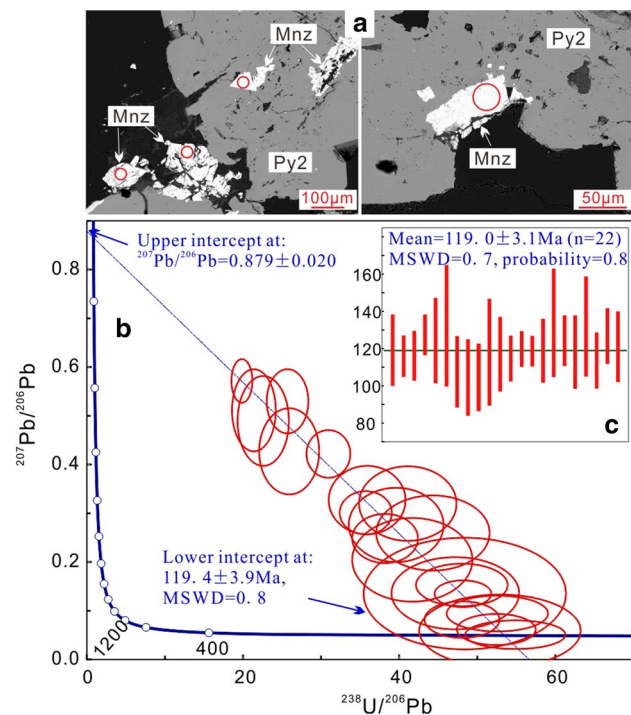
Fig. 9 a Representative monazite crystals, coexisting with pyrite. **b, c** The U–Pb Tera–Wasserburg Concordia diagram and the [207]Pb-corrected [206]Pb/[238]U weighted mean for monazite

on fluid inclusion assemblages (FIAs). The results are summarized in Table 2 and described below.

In stage I, type II fluid inclusions are dominant, with some type I inclusions. The melting temperatures of solid CO_2 (Tm_{CO_2}) for these inclusion types range from -58.2 to -56.6 °C. The melting temperatures for CO_2 clathrate (Tm_{clath}) of type IIa inclusions lie between 2.6 °C and 9.5 °C and the corresponding salinities are 1.0–12.4 wt.% NaCl equivalent. The total homogenization temperatures (Th_{tot}) range from 371 to 385 °C ($L + V$ to V or the critical state). For type IIb and IIc inclusions, the CO_2 clathrates melted at temperatures from 2.3 to 8.3 °C (Tm_{clath}), corresponding to salinities of 3.3–12.8 wt.% NaCl equivalent. Partial homogenization of CO_2 liquid and CO_2 vapor, consistently to liquid phase, occurred at 21.2–27.0 °C (Th_{CO_2}). The total homogenization temperatures (Th_{tot}) range from 279 to 329 °C ($L + V$ to L). Most of the type I inclusions have similar total homogenization temperatures (Th_{tot}) with coexisting type IIb and IIc inclusions, varying from 279 to 336 °C (Fig. 10i).

In stage II, all four types of fluid inclusion have been found, generally occurring as FIAs or coexisting with each other (Fig. 10j–l). Carbonic fluid inclusions in this stage have Tm_{CO_2} between -64.7 °C and -56.6 °C, indicating the presence of some impurities in the CO_2 phase. Laser Raman spectroscopy showed the impurities to be CH_4. Type
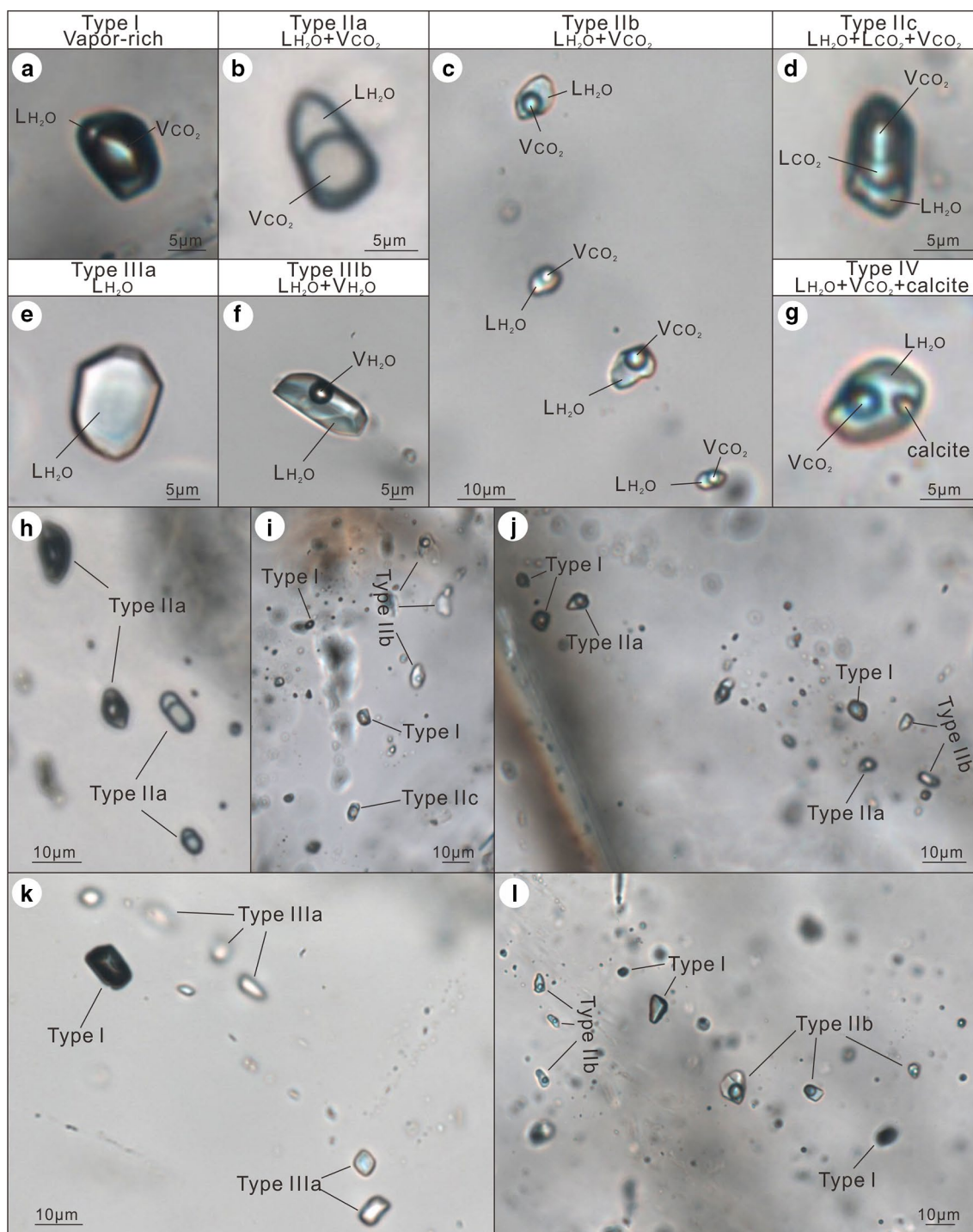
Fig. 10 Transmitted-light images of fluid inclusions. **a** Type I vapor-rich inclusion. **b** Type IIa two-phase H_2O–CO_2–NaCl inclusion with 60–40 vol.% carbonic phase. **c** Type IIb two-phase H_2O–CO_2–NaCl inclusions with 40–20 vol.% carbonic phase. **d** Type IIc three-phase H_2O–CO_2–NaCl inclusion. **e** Type IIIa one-phase H_2O–NaCl inclusion. **f** Type IIIb two-phase H_2O–NaCl inclusion. **g** Type IV daughter mineral-bearing H_2O–CO_2–NaCl inclusion. **h** Type IIa FIAs. **i** Three various fluid inclusion types occurred in the same plane of quartz from stage I. **j–l** Different fluid inclusion types coexist in quartz from stage II

I fluid inclusions have Tm_{clath} between 6.9 °C and 8.7 °C, corresponding to salinities of 2.6–5.9 wt.% NaCl equivalent, and Th_{tot} between 302 °C and 346 °C ($L + V$ to V). Type

IIa fluid inclusions have Tm_{clath} between 6.9 °C and 9.7 °C, corresponding to salinities of 0.6–5.9 wt.% NaCl equivalent. Two groups of Th_{tot} are observed in these inclusions ranging

Table 2 Summary of microthermometric data for fluid inclusions in quartz from the Zhuangzi gold deposit

Stage	Type	Tm_{CO_2}	Tm_{ice} (°C)	Tm_{clath} (°C)	Th_{CO_2} (°C)	Th_{total} (°C)	Salinity (wt.%)
I	1	−57.5 to −56.6		5.3–8.0		279–336	3.9–8.5
	2a	−58.2 to −56.6		2.6–9.5		371–385	1.0–12.4
	2b/2c	−57.2 to −56.8		2.3–8.3	21.2–27.0	279–329	3.3–12.8
II	1	−63.5 to −57.0		6.9–8.7		302–346	2.6–5.9
	2a	−62.1 to −57.6		8.9–9.9		348–367	0.2–2.2
		−62.9 to −56.7		6.9–9.7		292–343	0.6–5.9
	2b/2c	−62.7 to −56.6		5.1–9.4	28.8–30.6	284–346	1.2–8.8
	3b		−5.8 to −0.6			141–269	1.1–8.0
	4	−64.7 to −57.2		5.0–8.8		348–368	2.4–9.0

from 348 to 367 °C ($L+V$ to V or the critical state) and 292–343 °C ($L+V$ to V, few $L+V$ to L), respectively. Type IIb and IIc fluid inclusions have Tm_{clath} between 5.1 °C and 9.4 °C, corresponding to salinities of 1.2–8.8 wt.% NaCl equivalent. CO_2 generally homogenized to the liquid phase at 28.8–30.6 °C (Th_{CO_2}). The total homogenization temperatures (Th_{tot}) vary from 284 to 346 °C, concentrating around 300–336 °C ($L+V$ to L). Type IIIb fluid inclusions from the clustered quartz, forming in late stage II, yielded final ice melting temperatures (Tm_{ice}) of −5.8 to −0.6 °C, corresponding to salinities of 1.1–8.0 wt.% NaCl equivalent. The temperatures (Th_{tot}) of homogenization to the liquid phase are between 141 °C and 269 °C. In type IV inclusions, the daughter minerals persisted even at temperature as high as 600 °C (limit of the Linkam thermometric apparatus). They are carbonates, as determined by laser Raman spectroscopy, and likely represent accidental entrapment of the coexisting minerals. Nevertheless, the gas bubble disappeared at temperatures from 348 to 368 °C.

Discussion

Gold mineralization in the Jiaodong district is contemporaneous with a major tectonic transition from extension to transpression, associated with the abrupt change in the drifting direction of the subducting Pacific plate (Sun et al. 2007). Based on overgrowths, corrosion textures and morphological features of pyrite formed during gold mineralization period of Zhuangzi deposit, a clear paragenetic sequence for three types of pyrite can be defined, as well as their relationships with gold, quartz veins, pyrrhotite, arsenopyrite, and minor chalcopyrite. The geochemical and textural features of pyrite preserve evidence for the evolution of the hydrothermal fluids and physicochemical environment over time. Furthermore, these characteristics, together with fluid inclusions in the laminated quartz veins, can provide information about the mechanisms of gold precipitation. The following discussion will address the formation mechanism of the different pyrite generations, the trace elemental variations, the relationship between gold and other minerals, sulfur isotopic characteristic and fluid inclusions studies, as well as the age of mineralization, in order to elucidate the evolution of ore-forming fluids.

Pyrite formation and ore-forming fluid evolution

The Py0 grains with irregular or elongated shape, silicate inclusion-rich and trace element-poor characteristics precipitated contemporaneously with the earliest pyrite–sericite–quartz alteration (Fig. 11). These pyrite grains are typically parallel to the strong foliation (Fig. 4a). The above observations indicate that the initial hydrothermal fluids would have had low concentrations of As, Au and Cu, and the Py0 was precipitated in a compressive condition or experienced later shearing deformation.

After Py0 formation, oscillatory-zoned Py1, accompanied by a few fine quartz grains, precipitated during stage I mineralization (Fig. 11). Oscillatory zoning in pyrite has been documented in many gold deposits, where it was attributed to crystallographic incorporation of trace elements controlled by growth rate (Barker and Cox 2011; Fougerouse et al. 2016), and to chemical evolution of the hydrothermal fluid (Barker et al. 2009; Peterson and Mavrogenes 2014). In general, growth-rate-controlled incorporation would not cause changes in major elements during a single hydrothermal event, inconsistent with the zoning of S in Py1 (Fougerouse et al. 2016; Fig. 7c). Variations in the bulk fluid composition from multiple hydrothermal events usually cause several stages of sulfide precipitation with distinct sulfur isotopes, irregular boundaries and/or corrosion textures between alternating bands (Barker et al. 2009; Peterson and Mavrogenes 2014). None of these features is observed in the oscillatory zoning of Py1, arguing against the model of multiple stages of precipitation. A number of physico-chemical changes in the fluid likely contributed to the formation of oscillatory zoning in pyrite, such as varying pressure, temperature and pH during boiling of the hydrothermal fluid (Velasquez et al. 2014). It provides a novel idea to discuss the formation of alternating bands in Py1.
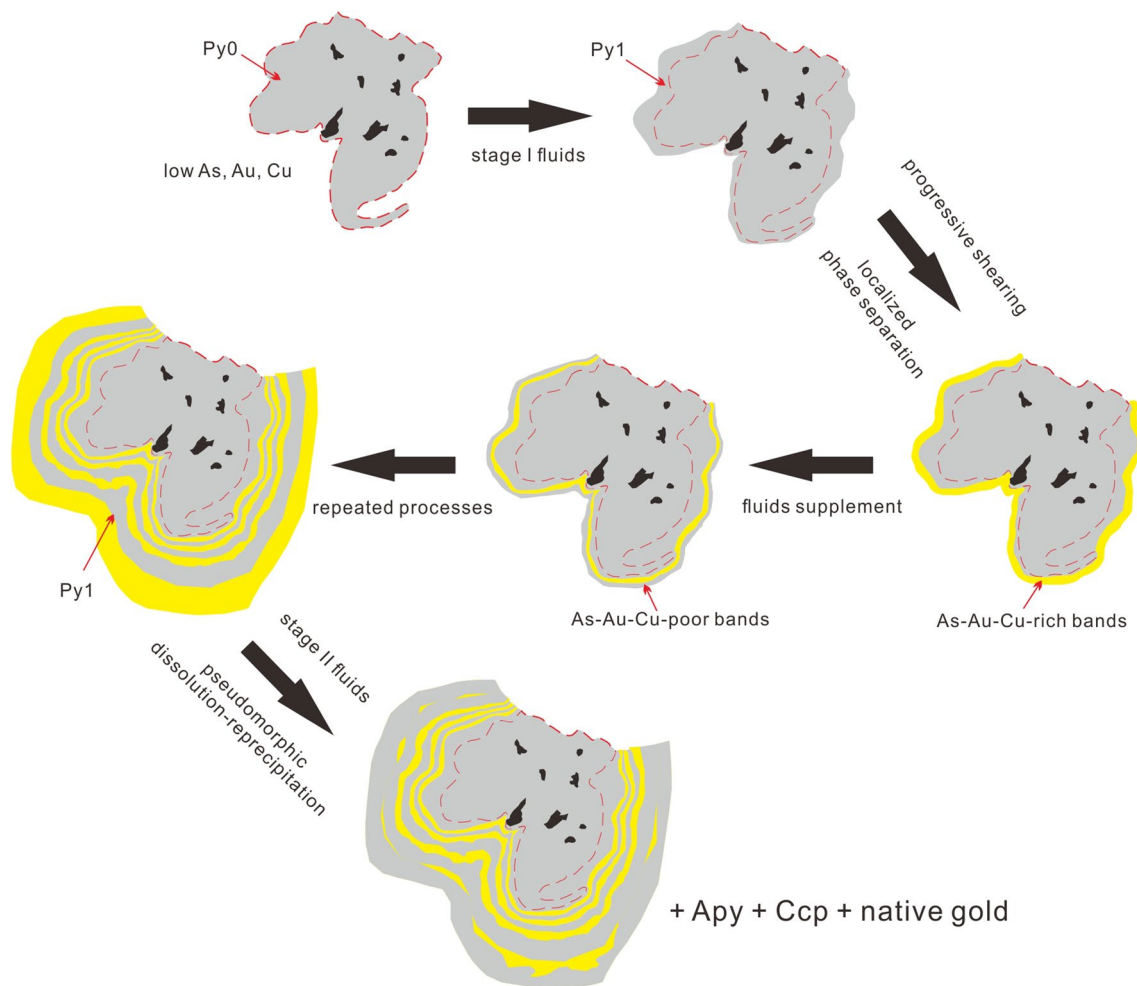
Fig. 11 A cartoon illustrating a model for pyrite formation at the Zhuangzi gold deposit. Py0 formed in the early pyrite–sericite–quartz alteration stage. It was followed by initial precipitation of Py1 at stage I. Progressive shear strain tends increased the fluid pressure in excess of the lithostatic pressure, creating an open space. A sudden drop of fluid pressure occurred, causing localized fluid phase separation, facilitating the formation of the As–Au–Cu-rich bright bands of Py1. With hydrothermal fluids supplement, the conditions became less favorable for phase separation, precipitating the As–Au–Cu–poor dark bands of Py1. Repeating this process resulted in the formation of oscillatory-zoned Py1. A new pulse of hydrothermal fluids was responsible for the formation of Py2, accompanied by arsenopyrite, chalcopyrite and native gold

Progressive shear strain tends to increase the fluid pressure in excess of the lithostatic pressure, creating open space or hydraulic fractures around the Py0 grains. This would have increased fluid flow forming quartz-pyrite veins and generated a sudden drop in fluid pressure, which, in turn, triggered localized phase separation of the hydrothermal fluids. The fluid phase separation is supported by the coexisting aqueous and carbonic inclusions with a significant variation in density (Fig. 10i). Recent studies have shown that arsenic, gold, and most other metallic elements largely favor partitioning into the liquid phase over the vapor phase at moderate temperatures like those of this study (< 400 °C; Kouzmanov and Pokrovski 2012, and references therein). Fluid phase separation would increase the concentrations of dissolved As, Au and Cu in the liquid phase and oversaturate the liquid with pyrite, forming the As–Au–Cu-rich bright bands of Py1 which commonly overgrows Py0. In addition, rapid decompression and fluid phase separation would decrease the temperature under adiabatic conditions, resulting in Au and As enrichment in pyrite. This is supported by thermodynamic equilibrium calculations reported by Pokrovski et al. (2002), Perfetti et al. (2008), and Kouzmanov and Pokrovski (2012). These calculations suggested that a decrease in temperature from 350 to 300 °C in ore-forming fluids would result in both Au and As enrichment in pyrite by a factor of 2–5. With more hydrothermal fluids supplied, the conditions became less favorable for phase separation and more similar to the primitive state in which the Py0 precipitated. The As–Au–Cu-poor dark bands of Py1 precipitated during this period, until the open space

was filled. Successive shearing deformation would have triggered precipitation of new As–Au–Cu-rich/As–Au–Cu-poor sequences. Consequently, formation of oscillatory-zoned Py1 was controlled by repeated opening and closing of the space around the already formed pyrite under a successive shearing deformation. According to this pattern, the chemistry of dark bands with low concentrations of As, Au and Cu in Py1 can approximately represent the initial signature of hydrothermal fluids in stage I, whereas the bright bands are the result of fluid phase separation. The gradual increase of trace elements in the bright bands from core to rim, and the presence of fine arsenopyrite inclusions in the outermost bands (Figs. 5, 7) are related to the accumulation of the residual fluid phase around the precipitating site.

Corrosion textures between Py1 and Py2 suggest episodes of dissolution and preclude the simple overgrowth of the pyrite from Py1 to Py2 (Fig. 7d). Similar textures have been documented by Fougerouse et al. (2016) who attributed them to fluid-mediated pseudomorphic dissolution–reprecipitation. This model can also explain the corrosion textures of pyrite in the Zhuangzi deposit. The Py1 cycling was followed by stage II mineralization with a new pulse of hydrothermal fluids, involving the pseudomorphic replacement of Py1 by Py2 (Fig. 11). The hydrothermal fluids in stage II also precipitated independent anhedral–subhedral clusters of Py2. The fact that Py2 usually contacts with the stage II quartz grains instead of altered rocks is consistent with the time of pseudomorphic replacement at stage II (Fig. 8e). Replacement of Au–As–rich Py1 by Au–As–poor Py2 might release gold and arsenic from Py1 into the hydrothermal fluids, and re-precipitate several arsenopyrite and native gold grains as inclusions in the same pyrite crystal, as well as just a short distance away. However, given the small pyrite/quartz ratio by mass, partial replacement of Py1 and concentrations of Au in Py1 (mostly below the detection limit of EPMA, < 614 ppm), the quantity of gold remobilized from Py1 is not enough to form economic mineralization. Abundant native and free gold grains co-precipitated with Py2 and quartz in stage II mineralization are likely the result of oversaturation and crystallization of Au-rich stage II ore-forming fluids in a later favorable condition. In addition, the presence of Po1 and Po2 after pyrite formation suggests a later decrease of sulfur fugacity (f_{S2}) in stage II mineralization (Lusk and Calder 2004). The high gold contents (0.08–0.34 wt.%) of pyrrhotite are consistent with Au-rich stage II hydrothermal fluids.

As noted earlier, laminations and clasts within the veins both contain altered minerals or clustered pyrite and are subparallel to the quartz vein margins which were emplaced subparallel to the lithological layers. This suggests that emplacement of the stage II veins due to preferential breakage along the altered rock layers resulted in the alignment of clasts and clustered pyrite under a shearing force. Successive

shearing-enhanced dissolution has removed most of the original quartz grains (Davis and Hippertt 1998), and led to the recrystallization of the residual quartz grains. This in turn resulted in the development of laminations within the vein.

Incorporation of arsenic and gold in pyrite

As discussed above, with the increasing concentration of dissolved As, Au and Cu during fluid phase separation, direct adsorption of these elements by Py1 can take place in unsaturated hydrothermal solutions. Simon et al. (1999a) proposed that arsenic in arsenian pyrite probably occurs as As^+, substituting for sulfur in the S_2^{2-} units. The substitution of As for S in the pyrite structure is supported by EPMA data which show a linear negative correlation (Fig. 6a). Considering the consistent variations of As, Au and Cu and homogeneous distribution of invisible gold in each band except the corners, Au most likely behaves similarly to As^+ in the lattice of pyrite, where it is incorporated as solid solution (Au^+) instead of discrete or clustered nanoparticles. The high As–Au contents in the corners of the pyrite crystals are remarkable (Fig. 7b, d, e), accompanying with low S contents (Fig. 7c). This localized As–Au enrichment cannot be related to the intragrain diffusion model where major element compositions remain unchanged, instead it may be due to distinct crystallographic orientations within pyrite (Reddy and Hough 2013; Fougerouse et al. 2018). However, the exact mechanism(s) of Au incorporation into pyrite is still poorly understood. The contents of invisible gold show a positive relationship with arsenic in the As-rich overgrowth zones, while the As-poor zones contain less or no gold. This phenomenon supports the common opinion that As-rich sulfides play a role in scavenging Au^+ (e.g., Fleet and Mumin 1997; Simon et al. 1999b).

Several mechanisms explaining the significance of arsenic have been invoked: (1) gold and arsenic might be present in dissolved Au–As–S complexes, such as $Au(AsS_3)^{2-}$ or $Au(AsS_2)^0$, and be adsorbed together (Clark 1960; Simon et al. 1999b and references therein); (2) the nonstoichiometric substitution of AsS^{3-} for S_2^{2-} in the pyrite lattice, causing the entry of an Au^+ ion into the distorted Fe^{2+} site or deficiency (Simon et al. 1999a, b); (3) surface electrochemical reactions facilitated by As coatings (e.g., Maddox et al. 1998); (4) chemisorption of Au complexes [e.g., $Au(HS)^0$ or $Au(HS)_2^-$] on As-rich and Fe-deficient pyrite surface (e.g., Fleet and Mumin 1997). The absence of hematite and sulfate in this study indicates that the hydrothermal fluid was H_2S dominated during pyrite crystallization; therefore, gold was likely transported as bisulfide complexes [e.g., $Au(HS)^0$ or $Au(HS)_2^-$; Williams-Jones et al. 2009]. Thus, the incorporation of Au as Au–As–S complexes can be ruled out, but the applicability of other mechanisms still needs to be investigated. Nevertheless, all the mechanisms are consistent

with As modifying the surface properties of pyrite, making it more amenable for the incorporation of gold.

Potential source of sulfur in sulfides

Sulfides in the Zhuangzi gold deposit are dominated by pyrite with only minor pyrrhotite, chalcopyrite and arsenopyrite. Therefore, isotopic fractionation between sulfide pairs would have been negligible. Given the temperature range (279–385 °C), low f_{O2} [the pyrite–pyrrhotite buffer in Ohmoto (1972)] and weak acidity (pH 3–5, Li et al. 2013) of hydrothermal fluids, the sulfur isotopic signature of pyrite can reasonably represent the bulk sulfur isotopic composition of ore-forming fluids (Ohmoto 1972). The narrow range (+ 7.1 to + 9.4 ‰) and similarities of the sulfur isotopic compositions among Py0, Py1 and Py2 indicate that the multiple pulses of hydrothermal fluids were likely derived from a common reservoir. The isotopic data from Zhuangzi do not allow us to determine the nature of sulfur reservoir, but the $\delta^{34}S$ compositions are similar to other deposits in the Jiaodong gold district (Mao et al. 2008), suggesting a similar sulfur source. Previous research suggested that the sulfur and metals were directly exsolved from the same magma source (Fan et al. 2003; Li and Santosh 2014). Goldfarb and Santosh (2014) argued against this based on the spatial and temporal relationship of ores and magmatic rocks, comparison of sulfur values between ore-related sulfides and Mesozoic granitoids, alteration zoning, and ore fluid chemistry, proposing that the sulfur and gold could be sourced from either oceanic sediments or the serpentinized mantle. Using fluid composition and systematic C–D–O–S–Sr isotopic data, Deng et al. (2015) proposed that the source could be constrained to the enriched mantle wedge associated with the dehydration and desulfidation of the subducted paleo-Pacific slab. However, lead isotope signatures, much less radiogenic relative to the Phanerozoic mantle and plotted to the left of the Geochron, of ore sulfides elaborated by Tan et al. (2012) are inconsistent with such a model of the Mesozoic mantle wedge, and strongly imply that the source of Pb, by inference that of Au and possibly S, is the metasomatized Paleoproterozoic subcontinental lithospheric mantle. Importantly, the initial $^{207}Pb/^{206}Pb$ ratio of the studied monazite (0.879 ± 0.020; Fig. 9b) overlaps within error with the $^{207}Pb/^{206}Pb = 0.896$ measured on ore sulfides by Tan et al. (2012), making the Paleoproterozoic source more convincing.

There is a slight variation of sulfur isotopic compositions ($\delta^{34}S = + 7.9$ to $+ 9.4$ ‰) in a single pyrite grain (Fig. 6d). Except for the high value (+ 9.4 ‰) from the Py0 core, other data from the Py1 and Py2 bands have a very narrow range (+ 7.9 to + 8.4 ‰), suggesting a systematic decoupling from the trace elemental composition variations of which were controlled by localized pressure fluctuation and fluid phase separation as discussed above. Numerous studies have revealed that the sulfur isotopic compositions of hydrothermal sulfides are strongly affected by f_{O2}, pH, temperature and the composition of the parental fluids, but the pressure effect is minimal (e.g., Ohmoto 1972; Seal 2006). Consequently the localized pressure fluctuations and fluid phase separation were not enough to generate sulfur isotopic fractionation in oscillatory pyrite zones. Therefore, given the constant f_{O2}, pH and mineralization temperatures, the $\delta^{34}S$ values in the Zhuangzi gold deposit are mainly controlled by the sulfur isotopic compositions of the parent fluids.

Metallogenic environment and mechanisms of gold precipitation

It has been well established that the tectonic regime in the NCC was dominated by extension during the Early Cretaceous, associated with the formation of extensive magmatic rocks, rift basins and metamorphic core complexes (e.g., Fan et al. 2003; Zhu et al. 2012). Around 120 Ma, a short compressional event has been proposed in the Jiaodong area, as a response to an abrupt change in the drifting direction of the subducting Pacific plate (Sun et al. 2007; Deng et al. 2015; Yang et al. 2018). This compressional event is coeval with ages of most gold deposits in the Jiaodong gold district. Monazite associated with peak gold mineralization at Zhuangzi constrains the age of mineralization to ca. 119 Ma. The field and microscopic textural evidence, including laminated quartz veins, slickensides on the lamination planes, shear lenses, strong foliations and recrystallized quartz assemblages, are all consistent with the mineralization being controlled by a sinistral shearing deformation. Recent studies on the Hushan gold deposit which is also located in the Penglai–Qixia gold belt revealed a transition from compression to extension at ca. 120 Ma (Yang et al. 2018), suggesting that the short compressional event may have played a unique role in gold mineralization in the Penglai–Qixia belt as a whole and needs to be investigated further.

Fluid inclusion studies suggest that Py1 and fine-grained quartz in stage I were mainly precipitated between 279 °C and 385 °C from a H_2O–CO_2–NaCl dominated hydrothermal system with moderate salinity. In stage I, three types of fluid inclusions were identified within the same plane (Fig. 10i) and showed similar homogenization temperatures from 279 to 336 °C, interpreted to be products of fluid phase separation. This is consistent with the alternating precipitation of oscillatory-zoned Py1 and incorporation of invisible gold into the bright bands. In stage II, type IIa fluid inclusions with high temperatures (348–367 °C) record a new pulse of hydrothermal fluid. Evidence of fluid phase separation was more common in quartz grains from stage II, where primary type I, IIa, IIb and/or IIIa fluid inclusions coexist and have similar salinities, gaseous compositions and total homogenization temperatures of 300–336 °C (Fig. 10j–l).

The precipitation of pyrrhotite in late stage II suggests a decrease of H_2S activity and indirectly proves the occurrence of fluid phase separation. Studies of the Au–As–Fe–S system indicate that decreasing H_2S activity and oxygen fugacity, caused by fluid phase separation, can facilitate native gold precipitation (Zhang and Zhu 2017). Consequently we propose that the incorporation of invisible gold into Py1 was linked to local fluid phase separation in stage I and facilitated by arsenic, whereas the deposition of abundant native gold was induced by a new volume of Au-rich ore-forming fluids and triggered by more extensive fluid phase separation during stage II.

Conclusions

The Zhuangzi gold deposit in the Jiaodong district formed at ca. 119 Ma based on monazite U–Pb dating, and was controlled by sinistral shearing deformation. Both the mineralization age and shearing structures are associated with a short compressional event around 120 Ma, which was caused by the abrupt change in the drifting direction of the subducting Pacific plate and likely triggered gold mineralization in the Jiaodong gold district.

The textural and geochemical characteristics of zoned pyrites from the Zhuangzi gold deposit indicate that multiple pulses of hydrothermal fluids, derived from a common sulfur source, were involved in the mineralization. Three types of pyrite with distinct textures and geochemistry were identified. Py0 with low contents of As, Au, and Cu is contemporaneous with the early pyrite–sericite–quartz alteration and commonly occurs as cores of pyrite crystals. Py1 with characteristic oscillatory zoning of As, Au, and Cu formed at stage I. The oscillatory zoning is interpreted to be the result of pressure fluctuation and repeated local fluid phase separation around the pyrite crystal. Py2 commonly overgrows Py1 and is likely the product of pseudomorphic dissolution–reprecipitation at stage II.

During stage I, invisible gold was incorporated into the Py1 structure probably as solid solution (Au^+), which was facilitated by As^+. Repeated As–Au–Cu-rich and As–Au–Cu-poor bands were the results of periodic opening and closing of the space around pyrite, causing pressure fluctuation and local fluid phase separation in the hydrothermal fluid. Subsequent gold remobilisation caused by replacement of Au-rich Py1 by Au-poor Py2 attributed to part of the gold mineralization, but the largest mass of gold was introduced by the ore-forming fluids in stage II. The deposition of native gold was triggered by extensive fluid phase separation in ore-forming fluids under successive shearing deformation.

References

Aleinikoff JN, Schenck WS, Plank MO, Srogi L, Fanning CM, Kamo SL, Bosbyshell H (2006) Deciphering igneous and metamorphic events in high-grade rocks of the Wilmington Complex, Delaware: morphology, cathodoluminescence and backscattered electron zoning, and SHRIMP U–Pb geochronology of zircon and monazite. Geol Soc Am Bull 118:39–64

Barker SLL, Cox SF (2011) Oscillatory zoning and trace element incorporation in hydrothermal minerals: insights from calcite growth experiments. Geofluids 11:48–56

Barker SLL, Hickey KA, Cline JS, Dipple GM, Kilburn MR, Vaughan JR, Longo AA (2009) Uncloaking invisible gold: use of nano-SIMS to evaluate gold, trace elements, and sulphur isotopes in pyrite from Carlin-type gold deposits. Econ Geol 104:897–904

Chen L, Li XH, Li JW, Hofstra AH, Liu Y, Koenig AE (2015) Extreme variation of sulfur isotopic compositions in pyrite from the Qiuling sediment-hosted gold deposit, West Qinling orogen, central China: an in situ SIMS study with implications for the source of sulfur. Miner Deposita 50:643–656

Clark LA (1960) The Fe–As–S system—phase relations and applications. Econ Geol 55:1345–1381

Davis BK, Hippertt JFM (1998) Relationships between gold concentration and structure in quartz veins from the Hodgkinson Province, northeastern Australia. Miner Deposita 33:391–405

Deditius AP, Reich M, Kesler SE, Utsunomiya S, Chryssoulis SL, Walshe J, Ewing RC (2014) The coupled geochemistry of Au and As in pyrite from hydrothermal ore deposits. Geochim Cosmochim Acta 140:644–670

Deng J, Wang C, Bagas L, Carranza EJM, Lu Y (2015) Cretaceous–Cenozoic tectonic history of the Jiaojia Fault and gold mineralization in the Jiaodong Peninsula, China: constraints from zircon U–Pb, illite K–Ar, and apatite fission track thermochronometry. Miner Deposita 50:987–1006

Diamond LW (2001) Review of the systematics of CO_2–H_2O fluid inclusions. Lithos 55:69–99

Fan HR, Zhai MG, Xie YH, Yang JH (2003) Ore-forming fluids associated with granite-hosted gold mineralization at the Sanshandao deposit, Jiaodong gold province, China. Miner Deposita 38:739–750

Fan HR, Hu FF, Yang JH, Zhai MG (2007) Fluid evolution and large-scale gold metallogeny during Mesozoic tectonic transition in the Jiaodong Peninsula, eastern China. Geol Soc Lond Spec Publ 280:303–316

Fan HR, Feng K, Li XH, Hu FF, Yang KF (2016) Mesozoic gold mineralization in the Jiaodong and Korean Peninsulas. Acta Petrol Sin 32:3225–3238 **(Chinese with English abstract)**

Farquhar J, Cliff J, Zerkle AL, Kamyshny A, Poulton SW, Claire M, Adams D, Harms B (2013) Pathways for Neoarchean pyrite formation constrained by mass-independent sulfur isotopes. Proc Natl Acad Sci USA 110:17638–17643

Fleet ME, Mumin AH (1997) Gold-bearing arsenian pyrite and marcasite from Carlin Trend deposits and laboratory synthesis. Am Mineral 82:182–193

Fleet ME, MacLean PJ, Barbier J (1989) Oscillatory-zoned As-bearing pyrite from stratabound and stratiform gold deposits: an indicator of ore fluid evolution. Econ Geol Monogr 6:356–362

Fougerouse D, Micklethwaite S, Tomkins AG, Mei Y, Kilburn M, Guagliardo P, Fisher LA, Halfpenny A, Gee M, Paterson D, Howard DL (2016) Gold remobilisation and formation of high grade ore shoots driven by dissolution-reprecipitation replacement and Ni substitution into auriferous arsenopyrite. Geochim Cosmochim Acta 178:143–159

Fougerouse D, Reddy SM, Kirkland CL, Saxey DW, Rickard WD, Hough RM (2018) Time-resolved, defect-hosted, trace element mobility in deformed Witwatersrand pyrite. Geosci Front. https://doi.org/10.1016/j.gsf.2018.03.010

Goldfarb RJ, Santosh M (2014) The dilemma of the Jiaodong gold deposits: are they unique? Geosci Front 5:139–153

Hough RM, Butt CRM, Fischer-bühner J (2009) The crystallography, metallography and composition of gold. Elements 5:297–302

Kouzmanov K, Pokrovski GS (2012) Hydrothermal controls on metal distribution in porphyry Cu (–Au–Mo) systems. Soc Econ Geol Spec Pub 16:573–618

Li SR, Santosh M (2014) Metallogeny and craton destruction: records from the North China Craton. Ore Geol Rev 56:376–414

Li JW, Bi SJ, Selby D, Chen L, Vasconcelos P, Thiede D, Zhou MF, Zhao XF, Li ZK, Qiu HN (2012) Giant Mesozoic gold provinces related to the destruction of the North China craton. Earth Planet Sci Lett 349:26–37

Li XC, Fan HR, Santosh M, Hu FF, Yang KF, Lan TG (2013) Hydrothermal alteration associated with Mesozoic granite-hosted gold mineralization at the Sanshandao deposit, Jiaodong Gold Province, China. Ore Geol Rev 53:403–421

Li RC, Chen HY, Xia XP, Yang Q, Li L, Xu J, Huang C, Danyushevsky LV (2017) Ore fluid evolution in the giant Marcona Fe–(Cu) deposit, Perú: evidence from in situ sulfur isotope and trace element geochemistry of sulfides. Ore Geol Rev 86:624–638

Liu S, Hu RZ, Gao S, Feng CX, Yu BB, Qi YQ, Wang T, Feng GY, Coulson IM (2009) Zircon U–Pb age, geochemistry and Sr–Nd–Pb isotopic compositions of adakitic volcanic rocks from Jiaodong, Shandong Province, Eastern China: constraints on petrogenesis and implications. J Asian Earth Sci 35:445–458

Liu ZC, Wu FY, Yang YH, Yang JH, Wilde SA (2012) Neodymium isotopic compositions of the standard monazites used in U-Th-Pb geochronology. Chem Geol 334:221–239

Ludwig KR (2012) Isoplot/Ex, version 3.75. Spec Publ No. 5. Berkeley Geochronology Center, Berkeley, California

Lusk J, Calder BOE (2004) The composition of sphalerite and associated sulfides in reactions of the Cu–Fe–Zn–S, Fe–Zn–S and Cu–Fe–S systems at 1 bar and temperatures between 250 °C and 535 °C. Chem Geol 203:319–345

Ma WD, Fan HR, Liu X, Pirajno F, Hu FF, Yang KF, Yang YH, Xu WG, Jiang P (2017) Geochronological framework of the Xiadian gold deposit in the Jiaodong province, China: implications for the timing of gold mineralization. Ore Geol Rev 86:196–211

Maddox LM, Bancroft GM, Scaini MJ, Lorimer JW (1998) Invisible gold: comparison of Au deposition on pyrite and arsenopyrite. Am Mineral 83:1240–1245

Mao JW, Wang YT, Li HM, Pirajno F, Zhang CQ, Wang RT (2008) The relationship of mantle-derived fluids to gold metallogenesis in the Jiaodong Peninsula: evidence from D–O–C–S isotope systematics. Ore Geol Rev 33:361–381

Mikhlin Y, Romanchenko A, Likhatski M, Karacharov A, Erenburg S, Trubina S (2011) Understanding the initial stages of precious metals precipitation: nanoscale metallic and sulfidic species of gold and silver on pyrite surfaces. Ore Geol Rev 42:47–54

Mills SE, Tomkins AG, Weinberg RF, Fan HR (2015) Implications of pyrite geochemistry for gold mineralisation and remobilisation in the Jiaodong gold district, northeast China. Ore Geol Rev 71:150–168

Ohmoto H (1972) Systematics of sulfur and carbon isotopes in hydrothermal ore deposits. Econ Geol 67:551–578

Perfetti E, Pokrovski GS, Ballerat-Busserolles K, Majer V, Gibert F (2008) Densities and heat capacities of aqueous arsenious and arsenic acid solutions to 350 °C and 300 bar, and revised thermodynamic properties of As(OH)$_3$ (aq), AsO(OH)$_3$ (aq) and iron sulfarsenide minerals. Geochim Cosmochim Acta 72:713–731

Peterson E, Mavrogenes J (2014) Linking high-grade gold mineralization to earthquake-induced fault-valve processes in the Porgera gold deposit, Papua New Guinea. Geology 42:383–386

Pokrovski GS, Kara S, Roux J (2002) Stability and solubility of arsenopyrite, FeAsS, in crustal fluids. Geochim Cosmochim Acta 66:2361–2378

Qiu YM, Groves DI, McNaughton RJ, Phillips GN (2002) Nature, age, and tectonic setting of granitoid-hosted, orogenic gold deposits of the Jiaodong Peninsula, eastern North China Craton, China. Miner Deposita 37:283–305

Reddy SM, Hough RM (2013) Microstructural evolution and trace element mobility in Witwatersrand pyrite. Contrib Mineral Petrol 166:1269–1284

Reich M, Kesler SE, Utsunomiya S, Palenik CS, Chryssoulis SL, Ewing RC (2005) Solubility of gold in arsenian pyrite. Geochim Cosmochim Acta 69:2781–2796

Roedder E (1984) Fluid inclusions. Rev Mineral 12:644

Seal RRI (2006) Sulfur isotope geochemistry of sulfide minerals. Rev Mineral Geochem 61:633–677

Simon G, Huang H, Penner-Hahn JE, Kesler SE, Kao L (1999a) Oxidation state of gold and arsenic in gold-bearing arsenian pyrite. Am Mineral 84:1071–1079

Simon G, Kesler SE, Chryssoulis S (1999b) Geochemistry and textures of gold-bearing arsenian pyrite, Twin Creeks, Nevada: implications for deposition of gold in Carlin-type deposits. Econ Geol 94:405–421

Sun WD, Ding X, Hu YH, Li XH (2007) The golden transformation of the Cretaceous plate subduction in the west Pacific. Earth Planet Sci Lett 262:533–542

Tan J, Wei JH, Audétat A, Pettke T (2012) Source of metals in the Guocheng gold deposit, Jiaodong Peninsula, North China Craton: link to early Cretaceous mafic magmatism originating from Paleoproterozoic metasomatized lithospheric mantle. Ore Geol Rev 48:70–87

Tanner D, Henley RW, Mavrogenes JA, Holden P (2016) Sulfur isotope and trace element systematics of zoned pyrite crystals from the El Indio Au–Cu–Ag deposit, Chile. Contrib Mineral Petrol 171:33

Tera F, Wasserburg GJ (1972) U–Th–Pb systematics in three Apollo 14 basalts and the problem of initial Pb in lunar rocks. Earth Planet Sci Lett 14:281–304

Velasquez G, Beziat D, Salvi S, Siebenaller L, Borisova AY, Pokrovski GB, de Parseval P (2014) Formation and deformation of pyrite and implications for gold mineralization in the El Callao District, Venezuela. Econ Geol 109:457–486

Williams-Jones AE, Bowell RJ, Migdisov AA (2009) Gold in solution. Elements 5:281–287

Xie SW, Wu YB, Zhang ZM, Qin YC, Liu XC, Wang H, Qin ZW, Liu Q, Yang SH (2012) U–Pb ages and trace elements of detrital zircons from Early Cretaceous sedimentary rocks in the Jiaolai Basin, north margin of the Sulu UHP terrain: provenances and tectonic implications. Lithos 154:346–360

Xu HJ, Zhang JF, Wang YF, Liu WL (2016) Late triassic alkaline complex in the Sulu UHP terrane: implications for post-collisional magmatism and subsequent fractional crystallization. Gondwana Res 35:390–410

Yang JH, Zhou XH (2001) Rb–Sr, Sm–Nd, and Pb isotope systematics of pyrite: Implications for the age and genesis of lode gold deposits. Geology 29:711–714

Yang KF, Fan HR, Santosh M, Hu FF, Wilde SA, Lan TG, Lu LN, Liu YS (2012) Reactivation of the Archean lower crust: implications for zircon geochronology, elemental and Sr–Nd–Hf isotopic geochemistry of late Mesozoic granitoids from northwestern Jiaodong Terrane, the North China Craton. Lithos 146–147:112–127

Yang LQ, Deng J, Wang ZL, Guo LN, Li RH, Groves DI, Danyushevsky LV, Zhang C, Zheng XL, Zhao H (2016) Relationships between gold and pyrite at the Xincheng gold deposit, Jiaodong Peninsula, China: implications for gold source and deposition in a brittle epizonal environment. Econ Geol 111:105–126

Yang KF, Jiang P, Fan HR, Zuo YB, Yang YH (2018) Tectonic transition from a compressional to extensional metallogenic environment at ~120 Ma revealed in the Hushan gold deposit, Jiaodong, North China Craton. J Asian Earth Sci 160:408–425

Zhang HC, Zhu YF (2017) Genesis of the Mandongshan gold deposit (Xinjiang, NW China): T–P–f_{S2} and phase equilibria constraints from the Au–As–Fe–S system. Ore Geol Rev 83:135–151

Zheng YF (2008) A perspective view on ultrahigh-pressure metamorphism and continental collision in the Dabie–Sulu orogenic belt. Chin Sci Bull 53:3081–3104

Zhou JB, Wilde SA, Zhao GC, Zhang XZ, Zheng CQ, Jin W, Cheng H (2008) SHRIMP U–Pb zircon dating of the Wulian complex: defining the boundary between the North and South China Cratons in the Sulu Orogenic Belt, China. Precambrian Res 162:559–576

Zhu G, Niu ML, Xie CL, Wang YS (2010) Sinistral to normal faulting along the Tan–Lu fault zone: evidence for geodynamic switching of the East China Continental Margin. J Geol 118:277–293

Zhu G, Jiang DZ, Zhang BL, Chen Y (2012) Destruction of the eastern North China Craton in a backarc setting: evidence from crustal deformation kinematics. Gondwana Res 22:86–103

Zhu ZY, Jiang SY, Ciobanu CL, Yang T, Cook NJ (2017) Sulfur isotope fractionation in pyrite during laser ablation: implications for laser ablation multiple collector inductively coupled plasma mass spectrometry mapping. Chem Geol 450:223–234